

**TECHNIQUES FOR HIGH-SPEED TIME-RESOLVED DEVICE
CHARACTERIZATION**

By

Saurin Shah

B.A.Sc. University of Waterloo, Waterloo, Canada, 1993

A THESIS SUBMITTED IN PARTIAL FULFILLMENT OF
THE REQUIREMENTS FOR THE DEGREE OF
MASTER OF APPLIED SCIENCE

in

THE FACULTY OF GRADUATE STUDIES
DEPARTMENT OF ELECTRICAL ENGINEERING

We accept this thesis as conforming
to the required standard

THE UNIVERSITY OF BRITISH COLUMBIA

Dec. 1995

© Saurin Shah, 1995

In presenting this thesis in partial fulfilment of the requirements for an advanced degree at the University of British Columbia, I agree that the Library shall make it freely available for reference and study. I further agree that permission for extensive copying of this thesis for scholarly purposes may be granted by the head of my department or by his or her representatives. It is understood that copying or publication of this thesis for financial gain shall not be allowed without my written permission.

Department of Electrical Engineering

The University of British Columbia
Vancouver, Canada

Date 18 DEC., 95

Abstract

The objective of this thesis is to address two open issues in time-resolved measurements of electronic devices. The first is the ability to perform measurements close to the device under test: we report a new approach to recover temporally-overlapping incident and reflected signals near a device. The technique involves electro-optic measurement at two locations. With suitable time-domain or Fourier-transform processing, the measured waveforms can be decomposed into components propagating towards and away from the device. We show experimental results for coplanar structures.

In the second part, we have identified a new feature in measured signals that we can attribute to substrate waves excited photoconductively during electro-optic sampling on coplanar striplines. Measurements at several positions laterally displaced from the center of the transmission line show that this substrate signal is confined to the neighborhood of the electrodes when the substrate is thin. We also show that this feature, which can be an impediment to accurate S-parameter characterization, can be eliminated by delaying it out of the time window of interest.

Finally, the Appendix lists the fabrication steps and process parameters for a lift-off process used to fabricate some of the samples used in this project.

Table of Contents

Abstract	ii
List of Figures	vi
Preface	viii
Acknowledgment	ix
1 Introduction	1
1.1 Introduction to Thesis	1
1.1.1 Overview	1
1.1.2 Summary of Results	2
1.1.3 Outline of Chapter	2
1.2 The Need for High-Speed Measurement Techniques	3
1.3 Coplanar Interconnects	4
1.3.1 Coplanar Waveguide and Coplanar Striplines	4
1.3.2 Surface Waves on Grounded and Ungrounded Dielectrics	7
1.4 Electro-Optic Sampling System	11
1.4.1 The Pump/Probe Technique	11
1.4.2 High-Speed Sampler	14
1.4.3 Photoconductive Generator	15
1.4.4 Performance	18
1.5 Two Open Issues in Time-Resolved Device Characterization	21

1.5.1	Distinguishing Incident and Reflected Signals	21
1.5.2	Photoconductive Excitation	23
1.6	Outline of Thesis	24
2	Separating Temporally-Overlapped Incident and Reflected Signals	25
2.1	Introduction to Chapter	25
2.1.1	Background and Motivation	25
2.1.2	Summary of Results	26
2.1.3	Outline of Chapter	27
2.2	Time-Domain Approach	27
2.2.1	Theory	27
2.2.2	Experimental Verification	31
2.3	Fourier-Transform Approach	36
2.3.1	Theory	36
2.3.2	Experimental Verification	39
2.4	Experimental Considerations	43
2.5	Conclusions	46
3	Guided Substrate Waves Generated by Photoconductive Excitation	47
3.1	Introduction	47
3.1.1	Background and Motivation	47
3.1.2	Summary of Results	49
3.1.3	Outline of Chapter	50
3.2	Experiment	50
3.3	Results	51
3.4	Analysis	55
3.5	Conclusions	60

Bibliography

61

A Experimental Device Fabrication

65

List of Figures

1.1	Coplanar waveguide geometry and field distribution.	5
1.2	Coplanar stripline geometry and field distribution.	8
1.3	Surface waves on a dielectric slab	10
1.4	Surface waves on a grounded dielectric slab	12
1.5	Layout of the electro-optic sampling system	13
1.6	Sampling of electric field on the transmission line	15
1.7	Excitation of electrical signal	16
1.8	L-shaped photoconductive switch	17
1.9	Step-like waveform generation on LT GaAs	20
1.10	Pulse generation using wire bond	22
2.1	Illustration for separation using time-domain approach	28
2.2	Layout of the open circuit used as DUT	31
2.3	Results for open-circuit device.	33
2.4	Comparison between measured signals and reconstructed waveforms from recovered signals	35
2.5	Illustration of recovery of signals using Fourier-transform approach	37
2.6	Layout of the short circuit used as DUT	40
2.7	Results for short-circuit device	41
2.8	Comparison of Fourier-transform approach and time-domain approach	44
3.1	Photoconductively-sampled waveform showing back surface reflection	48
3.2	Sampled waveform showing the THz feature	49

3.3	Layout of coplanar stripline with photoconductive generator	50
3.4	Arrival time of the THz feature on samples with different substrate thicknesses	52
3.5	Measured THz signals for three substrate thicknesses.	54
3.6	Relative delay of the THz signal for various substrate thicknesses	57
3.7	Determination of critical thickness for the surface-wave-like mode	59

Preface

Parts of thesis have been, or will be, published under the following titles:

- **Chapter 2:**

- **Millimeter-Wave Time-Resolved Measurement Near a Discontinuity: Separating Temporally-Overlapped Incident and Reflected Signals,**

S. A. Shah, A. Zeng, W. S. Wong, M. K. Jackson, L. Pouliot, A. Lecours, and J. F. Currie, Accepted by IEEE Microwave and Guided Wave Letters. To be published in Volume 6, Number 2.

- **Separating Temporally-Overlapped Waveforms with Electro-Optic Sampling,**

S. A. Shah, A. Zeng, W. S. Wong, M. K. Jackson, L. Pouliot, A. Lecours, and J. F. Currie, submitted to Optical and Quantum Electronics, 1 Nov., 1995.

- **Chapter 3:**

- **Guided Substrate Waves in Photoconductive Generation,**

S. A. Shah, A. Zeng, M. K. Jackson, L. Pouliot, A. Lecours, and J. F. Currie, to be submitted to IEEE Microwave and Guided Wave Letters.

Acknowledgment

First, I would like to thank my supervisor, Dr. M. K. Jackson, for his patient and knowledgeable supervision.

I would like to thank my co-worker Andrew Zeng for his help in the lab. I would especially like to thank Mani Vaidyanathan for great friendship, and reviewing my publications. I would like to thank Benny Tsou for useful discussion about fabrication process and microwave during this project.

Some of the samples used in this project were supplied by Dr. J. F. Currie and his co-workers at Department of Engineering Physics, Ecole Polytechnique, Montreal. I am grateful to them for supplying the samples quickly.

Samples were also fabricated at the Department of Electrical Engineering and Department of Physics. I would like to thank Hiroshi Kato and Dr. N. Jaeger for providing me the facility for fabrication and guidance. I would also like to thank Dave for evaporating the metals on the samples and Dr. T. Tiedje for use of the Scanning Electron Microscope.

During this research I have been supported by the Natural Sciences and Engineering Research Council of Canada (NSERC). This work was also supported by (NSERC) under the individual research grants and the Networks of Centers of Excellence (Micronet) programs

Finally, I would like to thank my girlfriend, Shanthi, for her patience, concern about my health and providing dinners during long experimental days during this project.

Chapter 1

Introduction

1.1 Introduction to Thesis

1.1.1 Overview

This thesis describes techniques developed for high-speed characterization using time-resolved measurement methods like electro-optic sampling. High-speed active and passive devices are under development in a frequency range where applications of conventional measurement equipment is limited. Thus, alternate measurement techniques like electro-optic sampling are widely used. The work described in this thesis concerns two major open issues in time-resolved measurement methods: the extraction of signals from the measurements performed close to the device under test (DUT) and the properties of a THz signal generated by photoconductive excitation. The first part describes a novel technique developed to separate incident and reflected signals when measurements are performed close to the DUT. This method has implications for characterization of high-speed devices using time-resolved techniques like electro-optic sampling and photoconductive sampling. The second part describes a study of the properties of a THz signal generated by the photoconductive switch and elimination of the THz signal for accurate device characterization.

1.1.2 Summary of Results

One of the major contributions described in this thesis is the development of a technique to separate the incident and reflected signals when measurements are performed close to the DUT. This was accomplished by electro-optic sampling at two different locations on the transmission line close to the DUT. With suitable processing, the signals propagating towards and away from the device can be extracted from the measured waveforms. The theory was experimentally verified by using open-circuit and short-circuit as devices under test integrated with coplanar stripline.

This thesis also describes a study of an unanticipated high-frequency feature appearing in measured signals; the arrival time of this signal was later than that of the signal traveling on the transmission line. We have identified the source of the feature, the photoconductive switch, which is capable of generating THz bandwidth signals. The arrival time of the signal compared to that of the leading edge of the step-like signal traveling on the transmission line is related to the substrate thickness. Since the medium in which this THz signal propagates is the substrate, we have studied the guiding of the signal with on- and off-axis measurements on samples with varying thickness. Measurements show that the THz signal is guided underneath the transmission line in the substrate when the substrate is thin. Finally, we have effectively eliminated the THz signal so that it does not interfere with device characterization.

1.1.3 Outline of Chapter

The purpose of the Chapter 1 is to provide background information, introduce the topics to be discussed later in the remainder of the thesis and outline the rest of the thesis. Section 1.2 describes the motivation for using the time-resolved technique such as electro-optic sampling to characterize high-speed electronic devices. Section 1.3 describes the

coplanar transmission lines and surface waves on a dielectric. The electro-optic sampling method is described in Section 1.4. In Section 1.5, two open issues in time-resolved measurement techniques that will be addressed in the remainder of thesis are described. Finally, Section 1.6 describes the organization of the remainder of the thesis.

1.2 The Need for High-Speed Measurement Techniques

Currently, high-speed active devices are being developed for analog and digital circuits for applications in fiber-optic systems, and satellite communication. Fiber-optic systems operating at 10 Gbit/s are in production and systems with a transmission rate of 40 Gbit/s are in the research and development stage. The demand for other applications operating at high speed is increasing rapidly as well. In order to design systems operating at high speeds and to build test instruments for these systems, active devices such as high-speed bipolar transistors, modulation-doped field-effect transistors (MODFET), and heterojunction bipolar transistors (HBT) are under development with f_t and f_{max} as high as 340 GHz [1] and 455 GHz [2], respectively. These high-speed devices are integrated on an appropriate substrate by interconnecting them with transmission lines. The traditional microstrip transmission line has high attenuation and dispersion values at these high frequencies. Thus, alternate transmission lines like coplanar stripline and coplanar waveguide are being developed. In order to design circuits operating at high speed, it is essential to understand the operation of active devices and the guiding properties of their interconnections.

In order to develop physical understanding of the operation of the electrical devices, it is required to characterize them. Conventional characterization equipment like the network analyzer has a maximum bandwidth of 60 GHz for broadband measurement, and the sampling oscilloscope has a minimum risetime of approximately 5 ps. In addition, the

network analyzer is only capable of making small-signal quasi-static measurements. Since the conventional electrical measurement methods are limited in characterization of high-speed devices and interconnects that are under development, alternate optoelectronic methods based on the ultrafast lasers have been developed. Electro-optic sampling [3, 4] and photoconductive sampling [5, 6] are the most popular optoelectronic methods used to characterize high-speed active [7, 8] and passive devices [9, 10, 11]. The electro-optic system used for the development of techniques for time-resolved measurement presented in this thesis is briefly described in Section 1.4.

1.3 Coplanar Interconnects

1.3.1 Coplanar Waveguide and Coplanar Striplines

Coplanar interconnects consist of conductors in the same plane, typically on the top surface of a dielectric substrate. The coplanar waveguide (CPW) and coplanar stripline (CPS) are two widely-used planar transmission lines in millimeter-wave and microwave circuits. Coplanar transmission lines have an advantage over the microstrip line in that shunt devices can be easily integrated to have the connection with the ground plane on the same side of the dielectric.

Coplanar Waveguide

The coplanar waveguide was proposed by Wen [12], and consists of a center strip with two ground planes located parallel to the strip placed on the same side of the dielectric surface as shown in Fig. 1.1(a). The electric and magnetic field configurations in the quasi-static limit are shown in Fig. 1.1(b). A simple quasi-static analysis for CPW can be carried out as in Ref. [12] using conformal mapping to determine the phase velocity and characteristic impedance for the case when the dielectric substrate thickness is sufficiently large to be

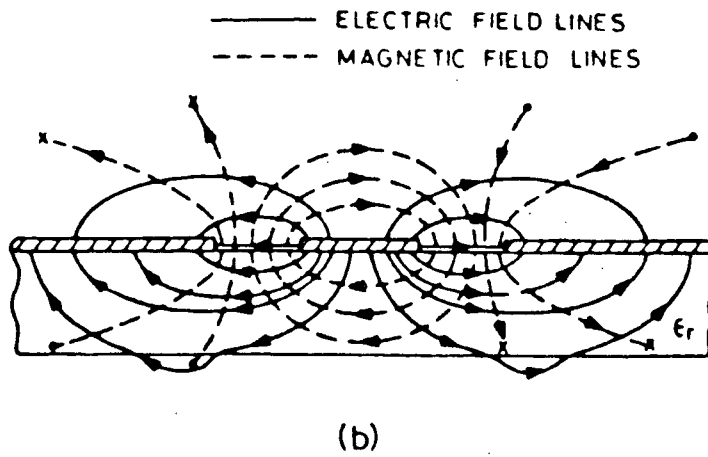
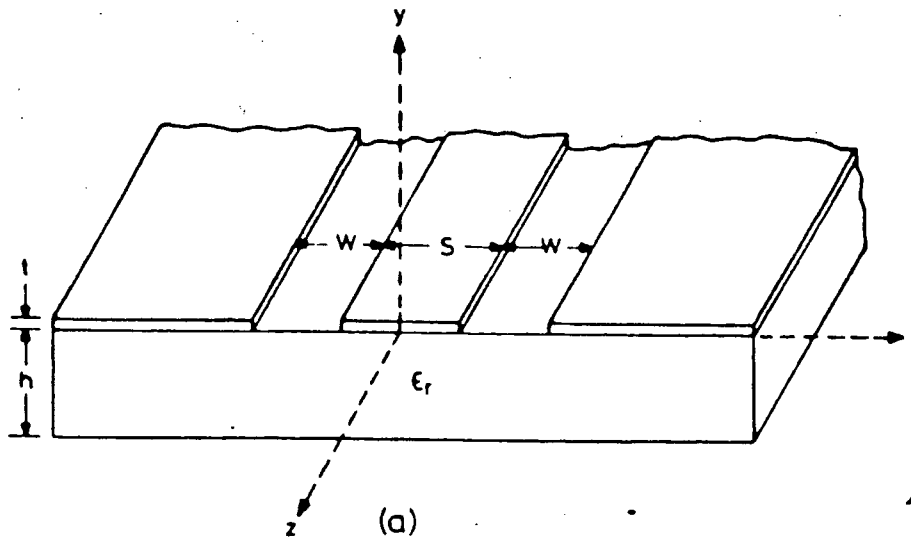


Figure 1.1: (a) Coplanar waveguide (CPW) geometry. (b) Electric and magnetic field distribution in CPW. (from Ref. [13])

considered infinite in the analytical model. It is also assumed that the thicknesses of the strip and ground plane electrodes are negligible. The phase velocity and characteristic impedance are given by

$$v_{cp} = \frac{c}{\sqrt{\epsilon_{\text{eff}}}} \quad (1.1)$$

$$Z_{ocp} = \frac{30\pi}{\sqrt{\epsilon_{\text{eff}}}} \frac{K'(k)}{K(k)} \quad (1.2)$$

where c is the velocity of light in free space, $K(k)$ is the complete elliptic integral of the first kind and $K'(k) = K(k')$. The effective dielectric constant is given by

$$\epsilon_{\text{eff}} = \frac{\epsilon_r + 1}{2}. \quad (1.3)$$

Since we assume that ϵ_{eff} is independent of frequency, the group velocity is equal to the phase velocity; this is the quasi-static approximation. The parameters k and k' for elliptic integral are defined as

$$k' = \sqrt{1 - k^2} \quad (1.4)$$

and

$$k = \frac{S}{S + 2W} \quad (1.5)$$

where S and W are the widths of the center electrode and the gap, as shown in 1.1(a). Accurate and simple expressions for the ratio of K/K' are available [13].

$$\frac{K(k)}{K'(k)} = \frac{1}{\pi} \ln \left[2 \frac{1 + \sqrt{k}}{1 - \sqrt{k}} \right] \text{ for } 0.707 \leq k \leq 1 \quad (1.6)$$

$$\frac{K(k)}{K'(k)} = \frac{\pi}{\ln \left[2 \frac{1 + \sqrt{k'}}{1 - \sqrt{k'}} \right]} \text{ for } 0 \leq k \leq 0.707 \quad (1.7)$$

Coplanar Stripline

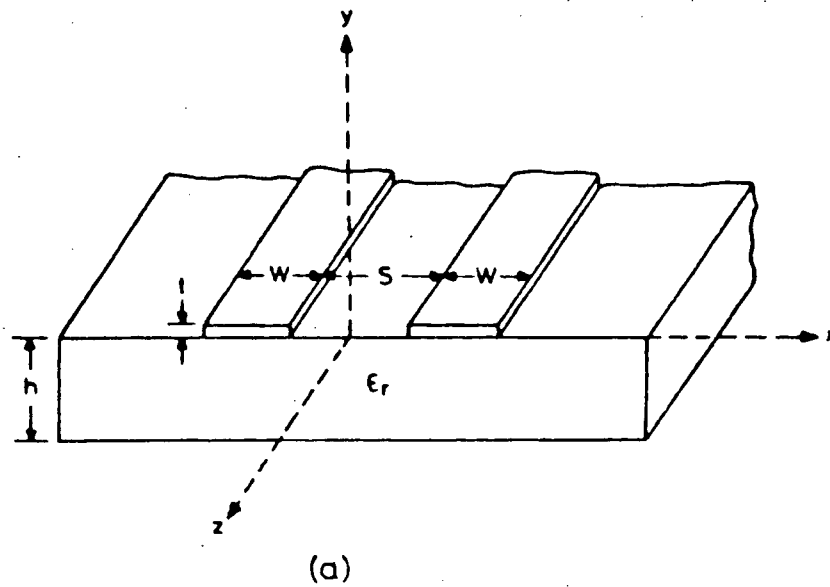
The coplanar stripline (CPS), which is complementary to the CPW transmission line, consists of two metallic strips running parallel on the same surface of the dielectric slab as shown in Fig. 1.2(a). The electric and magnetic field configurations are shown in Fig. 1.2(b). One can carry out an analysis similar to that used in the CPW case to determine the characteristic impedance and propagation velocity for the quasi-static approximation. Since CPS is complementary to CPW only equation 1.2 needs to be modified from set of equations (1.1)-(1.5). The characteristic impedance of the coplanar stripline is given by

$$Z_{ocs} = \frac{120\pi}{\sqrt{\epsilon_{\text{eff}}}} \frac{K(k)}{K'(k)}. \quad (1.8)$$

The velocity is given in this case by the same expression shown in Eq. 1.1.

1.3.2 Surface Waves on Grounded and Ungrounded Dielectrics

In this Section we examine surface waves on dielectrics, and their importance in coplanar interconnects. It is well known that a dielectric slab and a grounded dielectric slab are capable of guiding propagating electromagnetic energy. The energy is guided in the form of surface wave modes. Since the CPS and CPW are fabricated on a dielectric slab, one would expect that due to discontinuities formed by the connection of transmission lines with active and passive components with different characteristic impedance from the line that surface wave modes could be excited; this has been experimentally verified in Ref. [14]. The radiation of energy from coplanar mode to the surface wave modes can also occur even in the absence of discontinuities when the propagation constant of the coplanar transmission line is comparable to that of the surface wave modes [15, 16, 17, 18]. This leakage of energy causes attenuation of the guided wave on the coplanar lines at higher frequencies. Thus, it is essential to understand the properties of the surface wave



— ELECTRIC FIELD LINES
 - - - MAGNETIC FIELD LINES

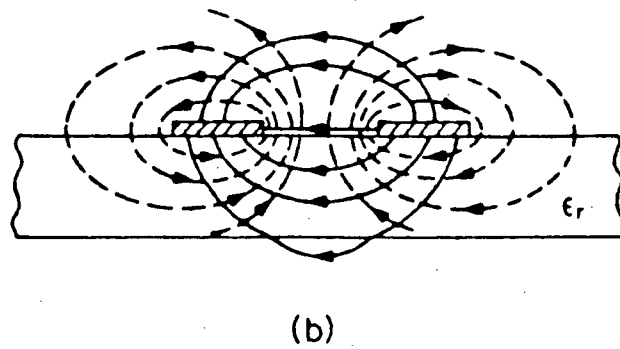


Figure 1.2: (a) Coplanar stripline (CPS) geometry. (b) Electric and magnetic field distribution in CPS.(from Ref. [13])

propagating in the slab with or without metallization to design coplanar interconnects for high-speed operation. In the following two subsections we review the properties of surface waves in these two cases.

Surface Waves on a Dielectric Slab

On ungrounded dielectric slabs, surface waves have fields that decay exponentially away from the dielectric surface, with most of the field contained in the dielectric or near the surface. The two lowest order transverse electric (TE) and transverse magnetic (TM) modes are shown in Fig. 1.3(a) for a dielectric slab of thickness h . They are TE_0 , TE_1 , TM_0 and TM_1 . The surface wave propagation constants calculated for a GaAs dielectric slab are shown in Fig. 1.3(b) for the two lowest-order TE and TM modes. The y-axis of the Fig. 1.3(b) is plotted with units of normalized propagation constant of the mode; where β is the frequency-dependent propagation constant of mode and k_0 is the wavenumber related to the wavelength of signal in the free-space, λ_0 .

$$k_0 = \frac{2\pi}{\lambda_0} \quad (1.9)$$

The frequency-dependent normalized propagation constant of a mode, β/k_0 , is often represented in the form of $\sqrt{\epsilon_{\text{eff}}}$, where ϵ_{eff} is the effective dielectric constant of the mode. The x-axis is plotted with units of normalized frequency, h/λ_0 ; where the wavelength of the signal in the free-space, λ_0 , is related to the frequency of the signal, f , given by

$$\lambda_0 = \frac{c}{f}. \quad (1.10)$$

It is clear from Fig. 1.3(b) that the two fundamental modes, TE_0 and TM_0 , have no cutoff frequency, and that higher-order modes appear as the frequency of the signal is increased. However, if the signal has constant frequency spectrum then the higher-order slab modes can also appear when the slab thickness is increased.

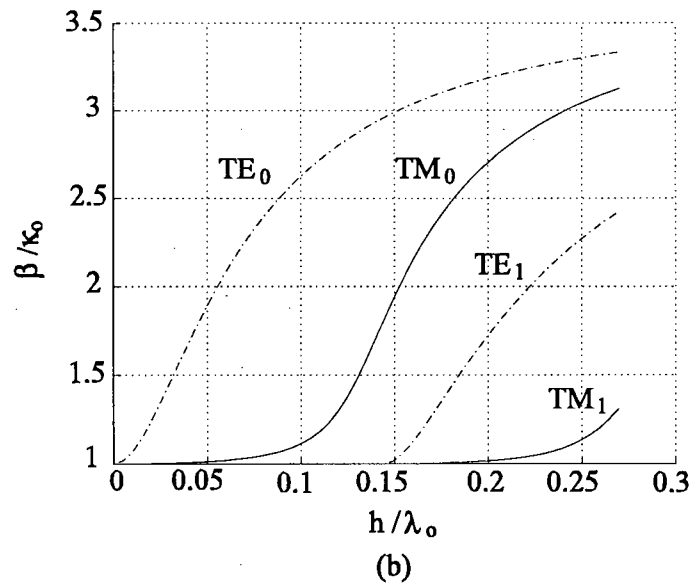
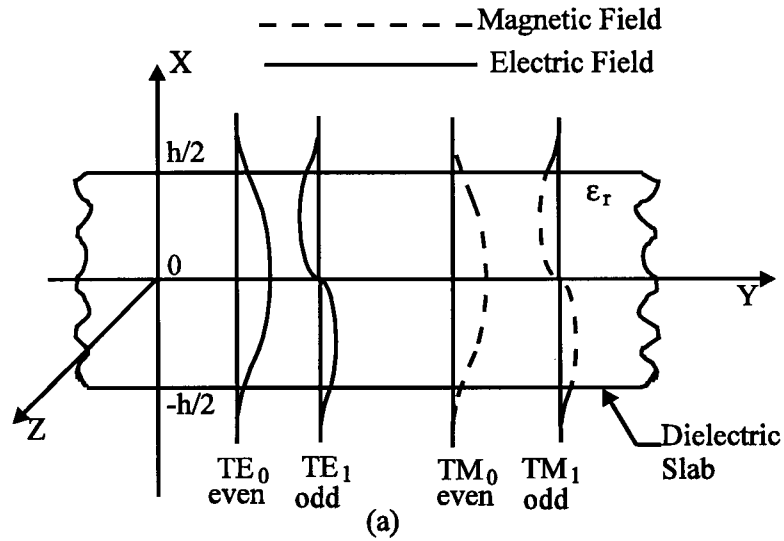


Figure 1.3: (a) Dielectric slab of thickness h with the four lowest order surface wave modes that may propagate. Field intensity is indicated as an excursion along y axis. (After Ref. [14]) (b) Surface wave propagation constants calculated for a GaAs dielectric slab with $\epsilon_r=13$.

Surface Waves on a Grounded Dielectric Slab

A grounded dielectric slab is a slab coated with metallic ground plane on one side. Similar to the ungrounded dielectric slab, the grounded dielectric slab can also guide the surface waves; these surface waves are different from those of an uncoated dielectric slab. However, it can be shown that the propagation constants for TE and TM modes of the grounded dielectric slab are same as those of odd TE and even TM modes of the ungrounded dielectric slab with twice the thickness of the coated dielectric slab. The two lowest-order modes of the grounded dielectric slab, TM_0 and TE_1 , are shown in Fig. 1.4(a). The propagation constants as a function of frequency for a metallized GaAs slab with thickness h are shown in Fig. 1.4(b). It is clear from Fig. 1.4(b) that TM_0 is the only mode that propagates at low frequency. As in the dielectric slab, the higher TE and TM modes of the grounded dielectric can also propagate as the frequency of the signal is increased.

1.4 Electro-Optic Sampling System

In this Section we describe the electro-optic sampling system used in the work presented in this thesis. Full details are given in Ref.[19].

1.4.1 The Pump/Probe Technique

The electro-optic sampling system is based on the pump/probe technique for time-resolved measurement of an electrical signal. The source of the pump and probe beams in our setup is a mode-locked Titanium-Sapphire laser which generates 150 fs pulses at a repetition rate of approximately 100 MHz. The laser output is split into two beams, referred to as pump and probe beams, using a beamsplitter as shown in Fig. 1.5. The pump beam is used to excite a fast electrical signal to the input of the device under test

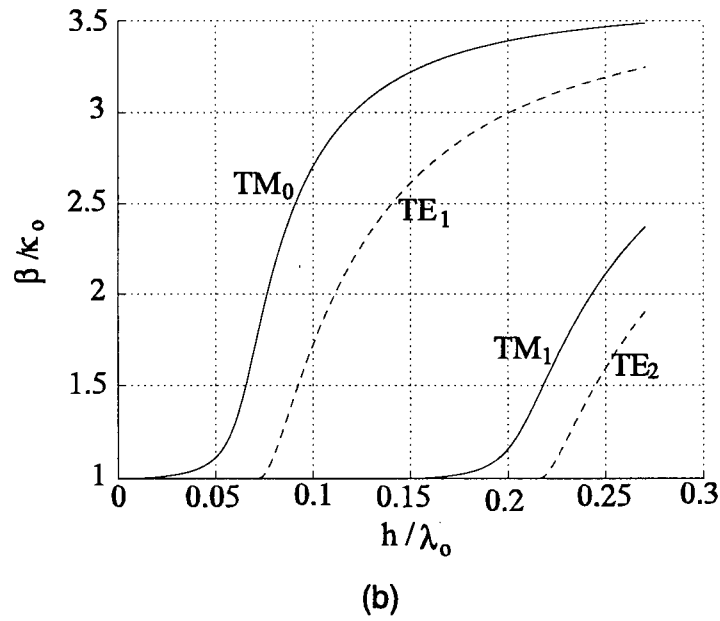
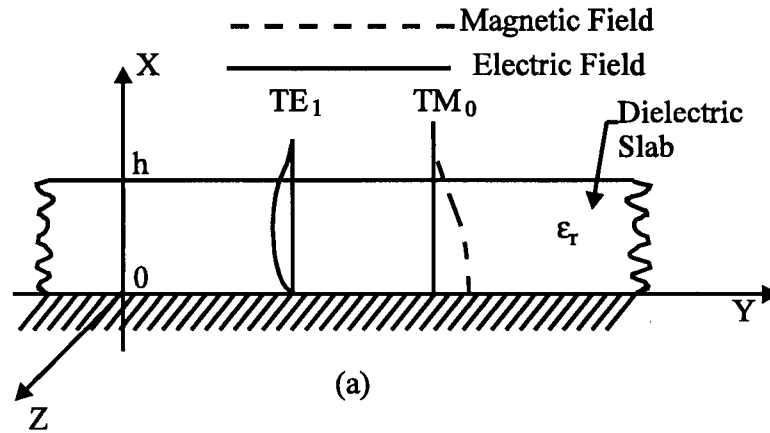


Figure 1.4: (a) Grounded dielectric slab of thickness h with the two lowest order surface wave modes that may propagate. Field intensity is indicated as an excursion along y axis. (After Ref. [14]) (b) Surface wave propagation constants calculated for a grounded GaAs dielectric slab with $\epsilon_r=13$ and thickness h .

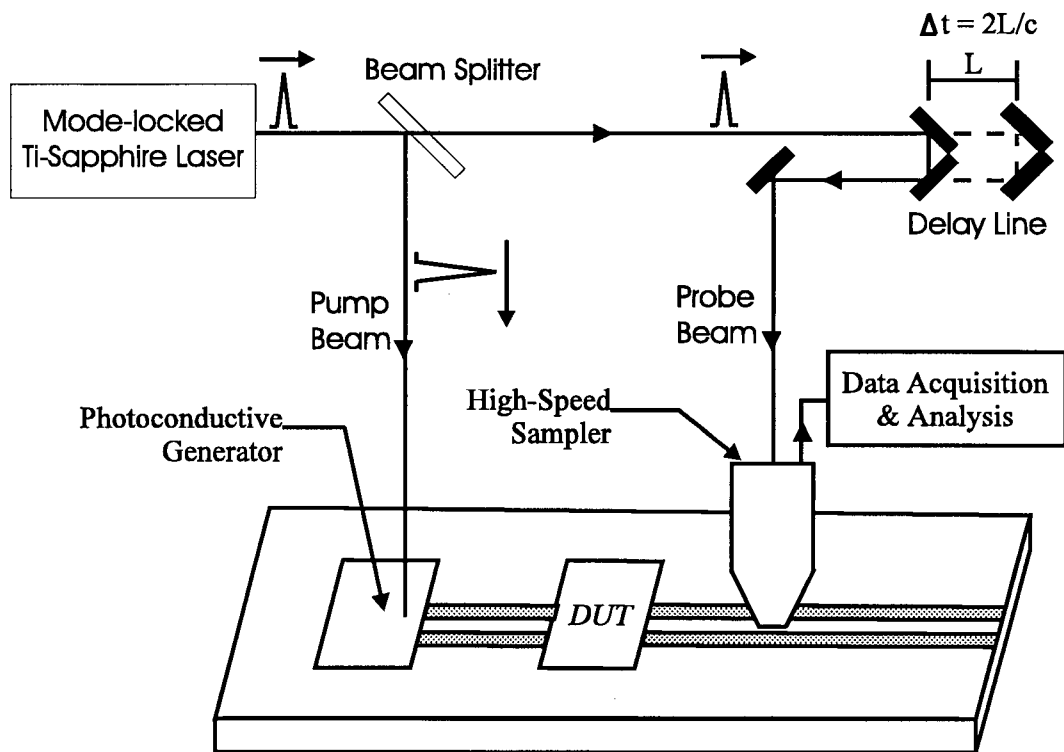


Figure 1.5: Layout of the electro-optic sampling system

on the transmission line using a photoconductive generator. The response of the device is measured using the high-speed sampler and the probe beam. The time at which the response is sampled is determined by the path lengths traveled by the pump and probe beams from the beamsplitter to the photoconductive generator and sampler, respectively. The function of the delay line is to time-delay the probe beam relative to the electrical signal to be measured. By varying the relative delay between pump and probe using the delay line, the response can be determined at any desired time. The optical delay-line is made up of two mirrors mounted on a motorized translation stage whose position can be accurately controlled. Since the optical path through the delay line is in air, the delay Δt is related to the speed of light, c , and change in path length, ΔL , by

$$\Delta t = 2 \frac{\Delta L}{c}. \quad (1.11)$$

Since the pump and probe beams come from the same source at the beamsplitter both are perfectly synchronized, making electro-optic sampling a jitter-free measurement technique. The excitation and measurement bandwidths are determined by the photoconductive generator and the high-speed sampler which are described in the following two subsections.

1.4.2 High-Speed Sampler

The high-speed sampler must be capable of measuring an electrical signal with a probe pulse. The high-speed sampler used in the electro-optic sampling system is an electro-optic amplitude modulator consisting of a linear polarizer, an electro-optic transducer, a compensator and an analyzer as shown in Fig. 1.6. The propagating electrical signal on the transmission line results in the formation of fringing fields in the semiconductor as well as in the air above the electrodes. As the probe tip is positioned above the electrodes, this fringing field produces a change in the birefringence of the electro-optic

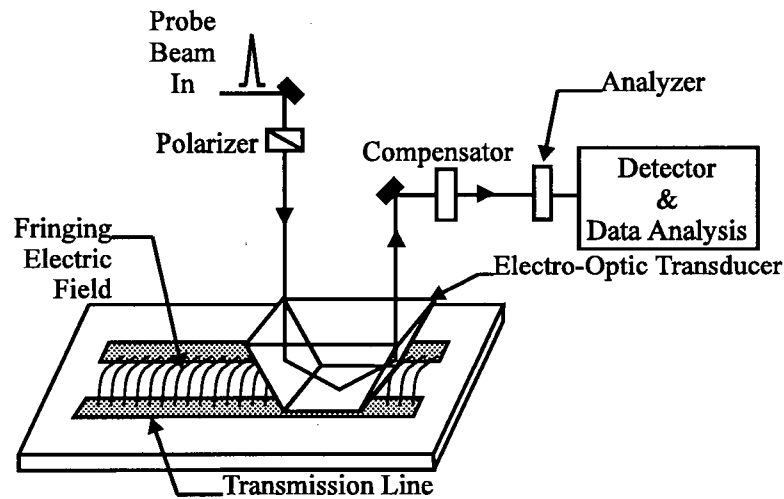


Figure 1.6: Sampling of electric field on the transmission line using probe beam

transducer through the electro-optic effect. The probe beam is polarized linearly before the tip and emerges from the tip with a polarization that is elliptical. The degree of ellipticity depends on the electric field in the tip at the instant the probe pulse passes through the tip, and therefore provides a time-resolved measure of the voltage between the coplanar electrodes [3]. The compensator and analyzer convert this measure of voltage recorded to a change in intensity of the probe beam. The probe beam is detected with photodetectors. The output of the photodetectors are processed using a lockin amplifier and other electronics before being recorded as a voltage on the transmission line as function of delay. The bandwidth of the high-speed sampler is limited by the lattice vibration frequency of the electro-optic transducer used; it is in excess of 1 THz for the LiTaO_3 electro-optic transducer used in our setup.

1.4.3 Photoconductive Generator

The photoconductive generator is an essential part of the electro-optic system, and generates an electrical signal on the transmission line when triggered by the pump beam. A gap photoconductive switch integrated with a coplanar stripline and biased with a

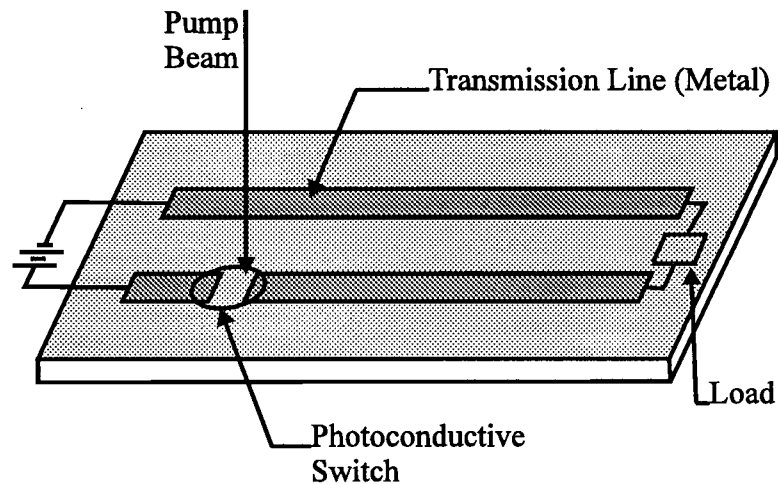


Figure 1.7: Excitation of signal by photoconductive switch controlled by pump beam

DC voltage is shown in Fig. 1.7. The photoconductive switch is fabricated on a semi-insulating substrate, and typically has a dark resistance of several megaOhm. Before the pump beam arrives the voltage across the load is close to zero due to the high resistance of the photoconductive switch. The pump beam short-circuits the gap for a short time by generating a flow of photoexcited carriers. This generates transient signals on the transmission line which propagate towards the load and towards the DC power supply. The risetime of the signal is determined by the pulsewidth of the pump beam along with the design of the photoconductive switch. The fall time is related to the carrier recombination lifetime of the material on which the switch is fabricated. One can generate a step-like signal by using a semi-insulating semiconductor with decay time of the order of 40 to 300 ps for semi-insulating GaAs. Photoconductive generators fabricated on photoconductive material damaged by ion-implantation with carrier lifetime in subpicosecond range is often used to generate pulse-like signals [20]. One can also decrease the carrier lifetime by growing a thin layer of GaAs on semi-insulating GaAs by molecular-beam epitaxy (MBE) under highly As-rich conditions at substantially lower temperature than the conventional ones near 580°C [21]. This low-temperature grown GaAs (LT GaAs)

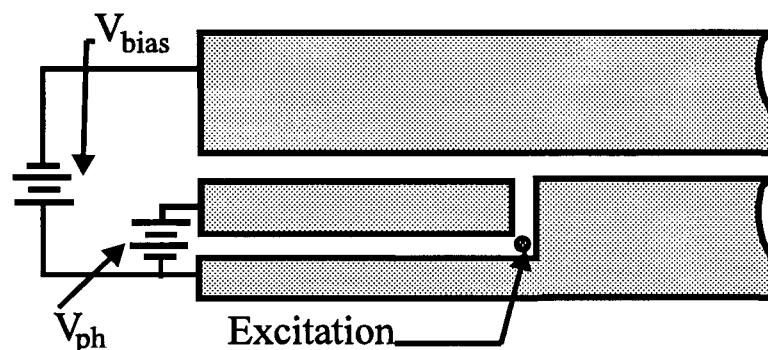


Figure 1.8: L-shaped photoconductive switch integrated with a coplanar stripline to allow biasing of active devices for characterization.

layer has large recombination-center density; as a result the carrier lifetime is reduced to the subpicosecond range.

For characterization of active devices, an L-shaped photoconductive switch integrated with a coplanar stripline is often used [7]. An accurate characterization of active devices such as transistors requires DC operation of the transistor at a bias point similar to that of a working circuit. S-parameter measurements or large-signal measurements are made by applying a stimulus signal on top of the biasing signal. Thus, independent control of the biasing supplies for the transistor and stimulus generator is required. The L-shaped photoconductive switch shown in Fig. 1.8 satisfies this requirement by having a separate DC power supply, V_{bias} , from the photoconductive switch power supply, V_{ph} , and therefore the stimulus generated by photoconductive excitation in the L-shaped gap is added to the biasing voltage.

The process responsible for generation of an electrical signal on the transmission line above is a very simple and widely-accepted view of a complex process. In fact, it is known that a photoconductive switch is capable of generating *both* guided and freely-propagating electromagnetic radiation with a THz bandwidth [22]. The radiation coupled into the

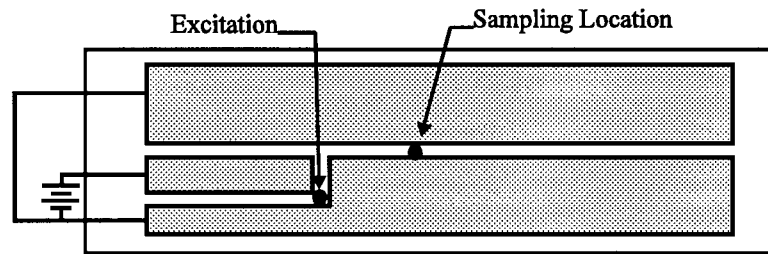
transmission line has been used for generation of electrical signals for high-speed measurement techniques such as electro-optic sampling [3] and photoconductive sampling [5] as described earlier in this subsection. In a similar configuration, the freely-propagating radiation generated has been used for free-space THz transmission measurements [23]. In this case, the radiation is emitted into the substrate in a cone shape perpendicular to the surface and collected by a lens attached to the back side of the substrate. In addition, as describe in Section 1.3.2 above, the substrate can support various propagating modes. In general, these modes can be excited by the photoconductively-generated transient. In fact, we have observed THz features travelling in the substrate along with the normal electrical signal traveling on the transmission lines; the details can be found in Chapter 3.

1.4.4 Performance

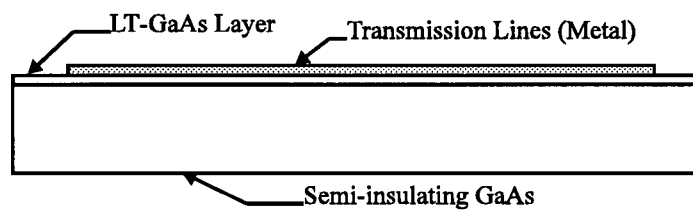
In the two previous subsections, it has been claimed that the excitation and measurement bandwidths of the electro-optic sampling system are in excess of 1 THz. Our standard electro-optic sampling setup restricts the minimum distance between the electro-optic transducer and the pump beam to 1.5 mm, thus attenuating and dispersing the high-bandwidth signal between the excitation and measurement locations. The risetime of the signal that can be measured 1.5 mm away from the photoconductive switch in our standard setup is approximately 2 ps. However, a signal has been measured by Zeng approximately 50 μm away from the photoconductive switch having a risetime of about 300 fs and FWHM of 500 fs by modification of the setup [19]; this demonstrates the system capability. The following subsections describe results of step-like waveform generation on an LT GaAs sample and generation of a broad bandwidth pulse by using a wire bond as examples to demonstrate normal performance of our measurement system.

Step-Like Waveform Generation

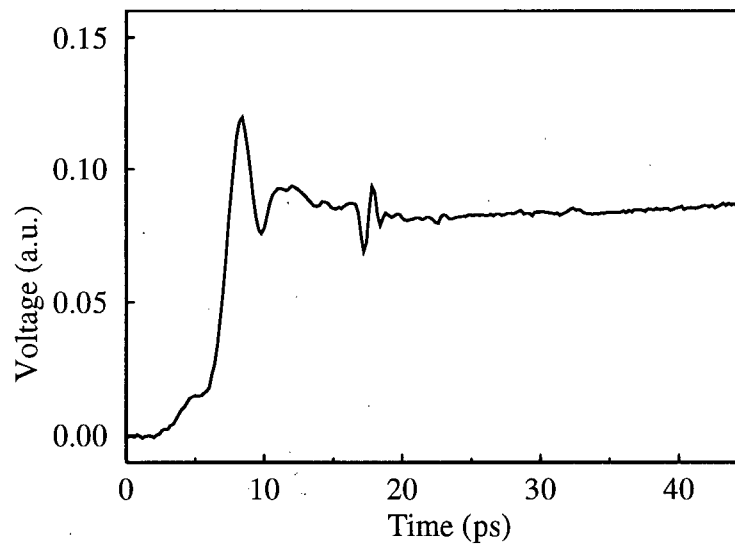
An L-shaped photoconductive switch integrated with coplanar strip was fabricated by using the standard lift-off process described in Appendix A. The pattern was defined on the $0.3\ \mu\text{m}$ thick LT GaAs grown layer on $500\ \mu\text{m}$ thick semi-insulating GaAs substrate. Figs. 1.9(a) and (b) show top and side views of the sample, respectively. In Fig. 1.9(c) we show a step-like waveform measured approximately $1.5\ \text{mm}$ away from the photoconductive switch. The 10 to 90 percent risetime of the signal is approximately $2\ \text{ps}$. The feature appearing at approximately $17\ \text{ps}$ is due to the THz signal guided by the substrate that will be discussed in Chapter 3. The signal remains at a constant level up to $45\ \text{ps}$. Since the LT GaAs photoconductive layer is expected to contain a large number of defects, it was expected that the signal generated should be pulse-like; however, a step-like waveform was observed. We can explain the observed result by considering the absorption of the pump beam power as a function of depth in the low-temperature and semi-insulating GaAs layers. The Ti-Sapphire laser in our experiment was operated at a wavelength around $830\ \text{nm}$ where the GaAs sample has an absorption length of approximately $1\ \mu\text{m}$, which is much longer than the $0.3\ \mu\text{m}$ thickness LT GaAs layer. Thus, we can expect that carriers would be excited in the thin LT GaAs layer with subpicosecond carrier lifetime as well as in the semi-insulating layer with long recombination carrier lifetime. As a result, the generated electrical signal should be the superposition of a fast pulse with short fall-time and a step-like signal with slow decay. The signal plotted in Fig. 1.9(c) exhibits this behavior. We can expect the ratio of amplitudes of the initial pulse signal and step-like signal to be comparable to the ratio of absorption in the $0.3\ \mu\text{m}$ and the GaAs substrate; the experimentally measured waveform shown in Fig. 1.9(c) is consistent with this.



(a)



(b)



(c)

Figure 1.9: Step-like waveform generation by excitation of photoconductive switch fabricated on $0.3/500 \mu\text{m}$ LT GaAs/GaAs. (a) Top view of the sample (b) Side view of the sample (c) Time-resolved measurement

Pulse Shaping using Wire Bond

In addition to damaging the semiconductor or growing it at low temperature to reduce the recombination carrier lifetime, the generated step-like waveform can be reshaped to have a pulse-like waveform [24]. Fig. 1.10(a) schematically shows placement of a wire bond close to a photoconductive switch fabricated on a semi-insulating substrate to reshape the step-like waveform generated. The measurement location was selected approximately 1.5 mm away from the photoconductive switch. The measured pulse is shown in Fig 1.10(b). It has a shape similar to a single cycle of a sine wave. The power spectrum of the measured pulse is shown in Fig 1.10(c) obtained by Fourier transformation of the time-domain waveform. The 3dB bandwidth of the measured pulse is in excess of 300 GHz. Thus, by simply using the wire bond as filter one can generate a wideband pulse which could be used to perform S-parameter measurements of devices.

1.5 Two Open Issues in Time-Resolved Device Characterization

1.5.1 Distinguishing Incident and Reflected Signals

In order to characterize an electrical device, it is essential to determine the excitation signal to the device and the response of the device. For example, conventional network analyzers used for S-parameter measurements have directional couplers attached to each port to separate the incident signal to the port from the reflected signal. In electro-optic sampling to make measurements of device input and output, the transient voltages are often measured on transmission lines connected to the device. Because electro-optic sampling is insensitive to the direction in which the measured signal is moving, signals propagating towards and away from the device cannot be distinguished if they overlap in time. For example, if a measurement is made at a fixed point on the input transmission line, the waveform will first show the incident signal as it propagates toward the device

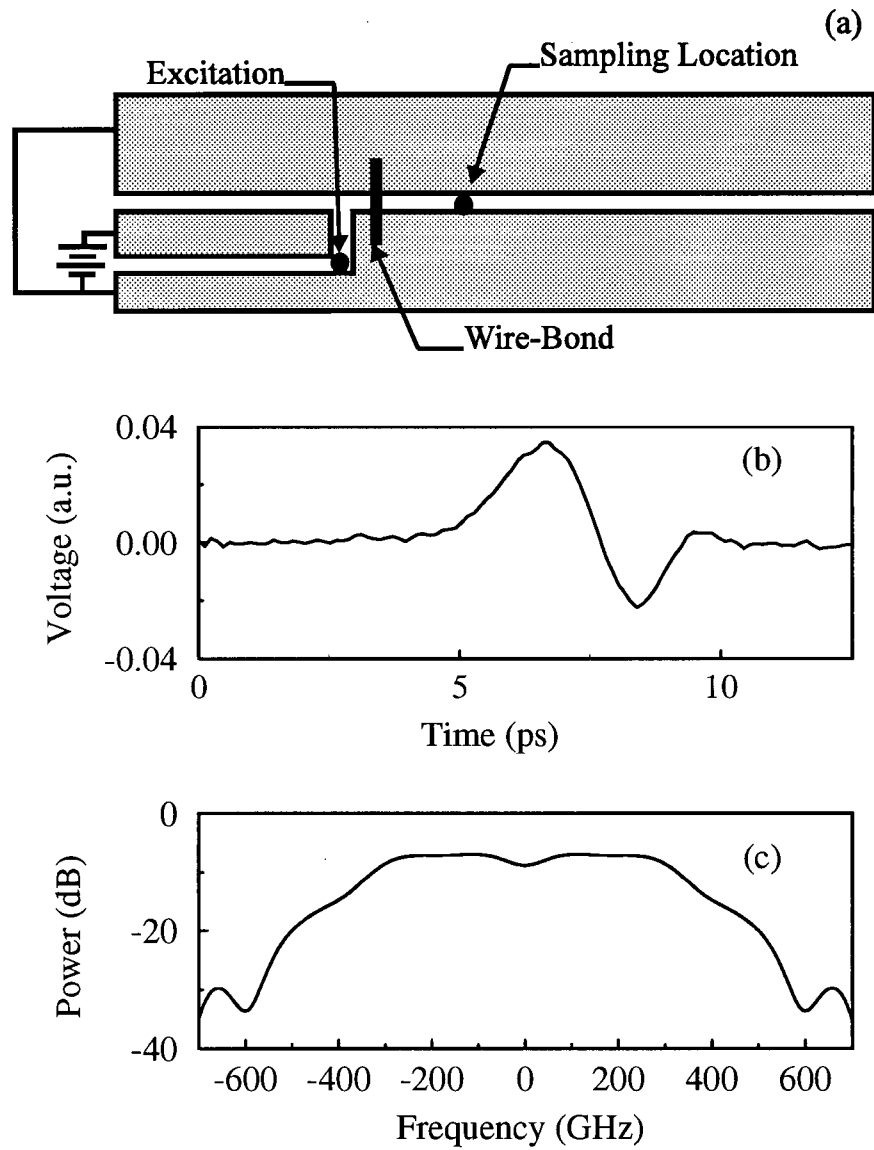


Figure 1.10: Generation of pulse using wire bond (a) Sample layout (b) Time-resolved measurement (c) Power spectrum of the measured signal

under test (DUT), followed by the reflected signal. If the incident signal duration is greater than the round-trip time from the sampling location to the DUT, the incident and reflected signals will temporally overlap and the two will be indistinguishable. Thus, the electro-optic sampling method lacks any mechanism to separate the incident and reflected signals when measurements are performed close to the DUT. In Chapter 2 we propose and demonstrate a novel technique which allows us to separate the incident signal from the reflected signal.

1.5.2 Photoconductive Excitation

In Section 1.4.3 we have stated that the photoconductive switch generates electromagnetic radiation with a THz bandwidth and that only part of this radiation couples into the transmission line mode. The substrate is capable of supporting modes that can guide this THz radiation as well. Thus, one would expect the generation of THz pulses in the substrate to accompany the generation of electrical signals propagating on the transmission lines. In fact, there has been a brief description of a feature observed by photoconductive sampling that was attributed to a reflection from the back surface of the substrate [25]. We have also identified a feature appearing after the initial peak of the step-like signal at approximately 17 ps as shown in Fig. 1.9(c). It is essential to determine the propagation properties of this signal because if the signal is guided by the transmission line as part of the coplanar stripline mode then this wide-bandwidth signal can be used to characterize devices. However, if the signal is not part of the coplanar stripline mode the device may not respond to this wide-bandwidth signal and it will interfere with the device characterization. In Chapter 3 we confirm the source of this feature as the photoconductive switch, and identify its propagation properties. In addition, we demonstrate a simple technique to effectively eliminate the feature.

1.6 Outline of Thesis

Chapter 2 addresses the issue of separation of incident and reflected signals from the overlapping time-resolved signals measured close to a device. The time-domain and Fourier-transform approaches developed to process the measured signals are first described theoretically with hypothetical examples. Both approaches are then experimentally verified by electro-optic sampling near open-circuit and short-circuit devices.

Finally, Chapter 3 describes a study of a newly identified feature in photoconductive generation. We have confirmed that the photoconductive switch is responsible for generating this feature, and that it is due to a THz signal traveling to the back surface of the sample before being reflected to the top. In order to study the propagation properties of this THz signal, samples with different thickness were prepared. The sampling performed on the transmission lines (on-axis) allowed us to look at the signal traveling on the transmission line as well as in the substrate. A lateral displacement of the electro-optic probe far away from the transmission line allowed us to sample (off-axis) the signal traveling in the substrate. By comparing on- and off-axis measurements for samples with different thicknesses we have concluded that the THz signal is confined closer to the coplanar electrodes for thin substrates.

Chapter 2

Separating Temporally-Overlapped Incident and Reflected Signals

2.1 Introduction to Chapter

2.1.1 Background and Motivation

As described in Chapter 1, electro-optic sampling is insensitive to the direction in which the measured signal is moving, and signals travelling towards and away from the device can not be distinguished if they overlap in time. In order to characterize an electrical device it is necessary to have the incident signal separated from the reflected signal. So it is essential to be able to separate incident and reflected signals when measured close to the device under test (DUT). Several approaches have been used to enable independent determination of the incident and reflected signals. The first, which is simple in principle, involves determining the incident signal on a different test fixture by replacing the DUT with a through line or combinations of open, short, and matched load [26]. This approach relies on being able to generate the same input signal reproducibly with two or more generators, which requires careful control of excitation position and focusing, and cannot be verified during the measurement. The second approach relies on having an incident signal duration small enough that the sampling location can be moved sufficiently far from the DUT to prevent temporal overlap. Generation of short incident signals requires reduction of carrier life-time of photoconductor by ion-implantation damage or appropriate choice of the photoconductive material, which may be inconvenient or impossible, especially when integrated on-wafer. In addition, the short pulses generated

are inconvenient in studies of large-signal switching, where step-like signals are desirable. Furthermore, locating the signal generator far from the DUT limits excitation bandwidth because transmission lines on the semiconductor substrates are highly attenuating and dispersive at millimeter-wave frequencies [27]. Finally, it is possible to use an attenuator as a directional device [28]; this approach depends on the quality of the broadband attenuator.

Even though the electro-optic sampling system has demonstrated excitation and measurement bandwidth in excess of 1 THz [4], the use of the system as time-domain network analyzer for small-signal characterization has been limited up to 500 GHz due to inability to separate incident and reflected waveforms when measured close to the DUT [29]. Thus, a technique is needed to recover temporally-overlapping incident and reflected signals while still allowing their measurement close to the DUT.

2.1.2 Summary of Results

To date, no technique has been reported to distinguish temporally-overlapping incident and reflected signals while still allowing their measurement close to the DUT. We propose a novel technique to accomplish separation of temporally-overlapping incident and reflected signals by making measurements at two locations. With suitable processing using either a time-domain approach or a Fourier-transform approach, the measured waveforms can be decomposed into components propagating towards and away from the DUT. We have successfully demonstrated the time-domain approach by separating overlapping incident and reflected signals using open circuit as DUT. We also have performed error analysis to determine the maximum separation between the two measurement locations required to successfully resolve signals with a 3dB signal bandwidth loss. We have extended the technique for separation of overlapping signals from the time-domain approach to a Fourier transform approach suitable for measured signals that can be Fourier

transformed. This extended method for separation of signals can be used to account for dispersion and attenuation between the two measurement locations if known. Furthermore, we show that the signals can be recovered without any loss of bandwidth for any separation between the two measurement locations. The Fourier-transform approach is demonstrated by separation of incident and reflected signals measured near a short circuit as DUT. Finally, we have compared recovered incident and reflected signals from the measurements on the short circuit sample using both approaches.

2.1.3 Outline of Chapter

The time-domain approach which can be applied to any input signal is described in Section 2.2, which also includes a description of the experimental setup, results obtained, and discussion of the results. The technique developed exclusively for signals that can be Fourier transformed is described in Section 2.3. A description of the experimental setup and a discussion of the results are also included in this Section. The factors in the experimental setup that critically affect the success of these approaches are described in Section 2.4. Finally, conclusions are summarized in Section 2.5.

2.2 Time-Domain Approach

2.2.1 Theory

To illustrate the technique involving only time-domain processing, hypothetical step-like signals measured for a DUT which is an open circuit are described below. In Figs. 2.1(a) and (b) we show the signals that would be observed at two positions between the generator and the DUT. Fig. 2.1(a) shows a typical signal $g_A(t)$ measured at location A: the incident step-like signal $f_{inc}(t)$ is followed later by a reflected signal $f_{ref}(t)$ from the DUT. The curve in Fig. 2.1(b) shows the signal $g_B(t)$ that would be observed at a location B closer

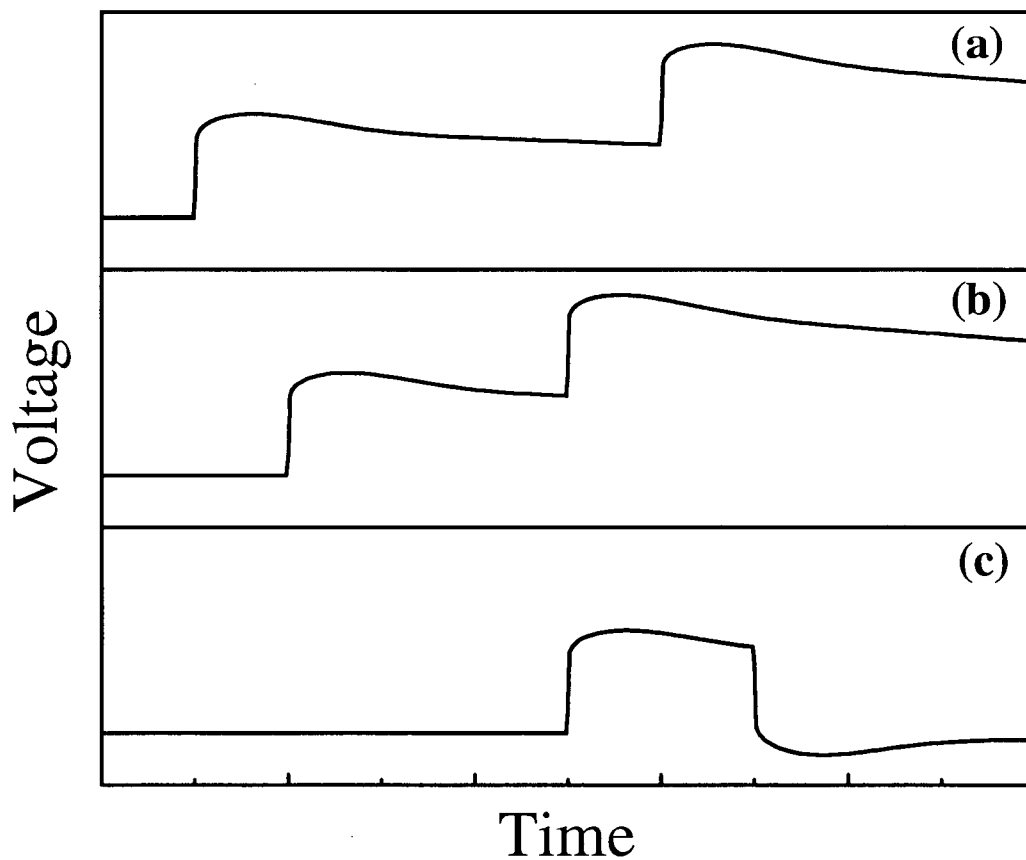


Figure 2.1: (a) and (b) *Hypothetical* waveforms that would be observed at two locations between the generator and an open-circuit device under test (DUT). The waveform in (b) would be sampled at a location closer to the DUT, and the waveform in (a) further from the DUT. (c) Waveform related to the reflected signal, obtained by subtracting the time-shifted waveform of (a) from the curve of (b) as described in the text.

to the DUT: the incident signal arrives slightly later, and the reflection slightly earlier. These signals can be expressed as

$$g_A(t) = f_{inc}(t) + f_{ref}(t) \quad (2.1)$$

$$g_B(t) = f_{inc}(t - \tau) + f_{ref}(t + \tau) \quad (2.2)$$

where the time-shift is $\tau = L/v$. The length L is the separation between location A and B and v is the propagation velocity on the transmission line. In writing equations (2.1)-(2.2) we have assumed that attenuation and dispersion between two measurement locations are negligible over the frequency range of interest. This means that the only difference between the signals measured at the two locations originates in the time shift due to propagation delay.

If the two sampling locations are close enough, then it is straightforward to recover both incident and reflected signals. For example, to recover the reflected signal $f_{ref}(t)$ from the data of Fig. 2.1(b), we can shift the $g_A(t)$ in time by τ so that the incident signal overlaps with the incident signal in the $g_B(t)$. Subtracting the time-shifted $g_A(t)$ from the $g_B(t)$ gives waveform $g_{diff}(t)$ shown in Fig. 2.1(c). It is easy to show that for small spatial separation that the curve $g_{diff}(t)$ of Fig. 2.1(c) is proportional to the derivative of the reflected signal $f_{ref}(t)$:

$$\begin{aligned} g_{diff}(t) &= g_B(t) - g_A(t - \tau) \\ &= f_{ref}(t + \tau) - f_{ref}(t - \tau) \\ &\approx 2\tau \frac{df_{ref}(t)}{dt} \end{aligned}$$

Thus, by numerical integration the reflected signal can be recovered. The incident component $f_{inc}(t)$ of the measured signal can be obtained in a similar way by removing the reflected signal during the subtraction process. The reflected and incident signals are

given by

$$f_{ref}(t) \approx \int_{-\infty}^t \frac{g_B(t') - g_A(t' - \tau)}{2\tau} dt' \quad (2.3)$$

and

$$f_{inc}(t) \approx \int_{-\infty}^t \frac{g_A(t' + \tau) - g_B(t')}{2\tau} dt' \quad (2.4)$$

We have used a finite difference approximation for the time-derivative. In order to determine the effect of this approximation process on the recovered signals let call $h_{ref}(t)$ the reflected signal recovered; ideally it would be identical to $f_{ref}(t)$. The recovered reflected signal $h_{ref}(t)$ is obtained from

$$\frac{dh_{ref}(t)}{dt} = \frac{f_{ref}(t + \tau) - f_{ref}(t - \tau)}{2\tau}. \quad (2.5)$$

One can determine a relationship between the recovered signal $h_{ref}(t)$ and the true reflected signal $f_{ref}(t)$ by Fourier-transforming Eq. 2.5 followed by simplifications. The resultant relationship in the frequency domain is given by

$$\frac{h_{ref}(\omega)}{f_{ref}(\omega)} = \frac{\text{sinc}(\omega\tau)}{\omega\tau}. \quad (2.6)$$

Eq. 2.6 shows that the process of recovering signals has a low-pass filtering effect on the recovered signals with a frequency dependence $\text{sinc}(\omega\tau)$. From this, the 3dB bandwidth of the recovery process is $0.22/\tau$. The accuracy of the recovered signals can be increased by decreasing the distance between measurement locations, provided the experimental signal-to-noise ratio is adequate.

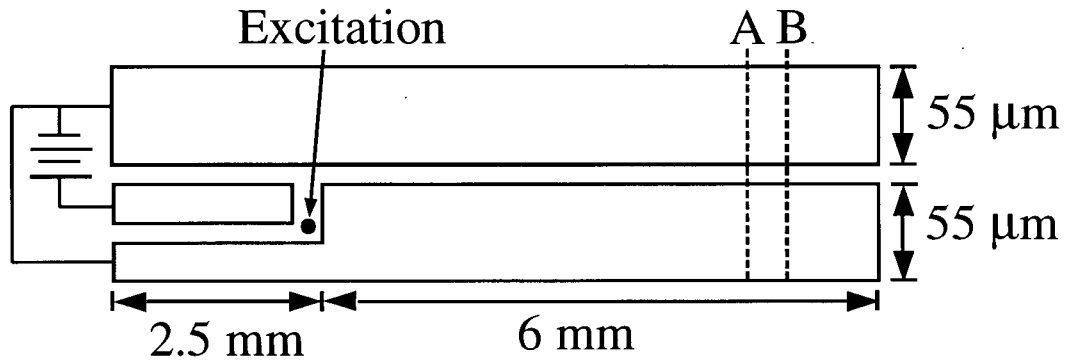


Figure 2.2: Layout of coplanar-stripline test-structure with open-circuit at the end, and a photoconductive generator. All gaps are $5 \mu\text{m}$.

2.2.2 Experimental Verification

Experimental Arrangement

The open circuit DUT shown in Fig. 2.2 was photolithographically defined on a $425 \mu\text{m}$ thick semi-insulating GaAs substrate. The coplanar stripline electrode pattern is one that has been used to allow biasing of active devices [7, 8]; they were patterned by lift-off processing of an electron-beam evaporated bilayer of 10 nm of Titanium followed by 200 nm of Gold. Electro-optic measurements were made with 150 fs optical pulses, and an external LiTaO_3 electro-optic sampling tip with a footprint approximately $220 \mu\text{m}$ square. While many measurements using external sampling tips have been made with the tip in direct contact with the transmission line, it has recently been shown that the impedance mismatch due to the LiTaO_3 tip can cause significant distortions of the measured results [30, 31]. Therefore, we used the non-contact configuration with an air gap between electro-optic transducer and transmission line of approximately $7 \mu\text{m}$ for all measurements.

Results

In Fig. 2.3 we show the data measured for the open-circuit sample described above, and the recovered incident and reflected signals. The solid line of Fig. 2.3(a) shows the signal $g_A(t)$ measured at location A of Fig. 2.2, which is located $650 \mu\text{m}$ from the open circuit DUT. The step-like incident signal $f_{inc}(t)$ starting at about 5 ps is followed by the reflection $f_{ref}(t)$ which starts at approximately 17 ps. The dashed line in Fig. 2.3(a) shows the signal $g_B(t)$ measured at location B of Fig. 2.3, which is $50 \mu\text{m}$ closer to the open circuit DUT than A. The 3dB bandwidth for the recovery technique for $L = 50 \mu\text{m}$ separation is 500 GHz, which is much larger than the 100 GHz bandwidth of the signal generated. As expected, the incident signal is slightly delayed and the reflected signal is slightly advanced by the change in location. The sampling period was chosen to be 150 fs. In order to aid the numerical processing, the measured waveforms were interpolated by four points between each of the measured data points.

The recovery process for the reflection signal described by (2.3) requires that the waveform $g_A(t)$ measured at location A to be time-delayed to cancel the incident component from the measured signal $g_B(t)$. The time-shift, τ , was chosen to give the best cancellation. The propagation velocity calculated from this time shift compares well with the measured velocity. This subtraction process was followed by numerical integration to obtain the signal reflected from the device, which is shown in Fig. 2.3(b) as a dashed line. The incident signal is recovered with a similar procedure, and is shown in Fig. 2.3(b) as a solid line.

Discussion

As expected, the retrieved incident and reflected signals of Fig. 2.3(b) show features evident in the measured data of Fig. 2.3(a) where both signals overlap. The 10 to 90

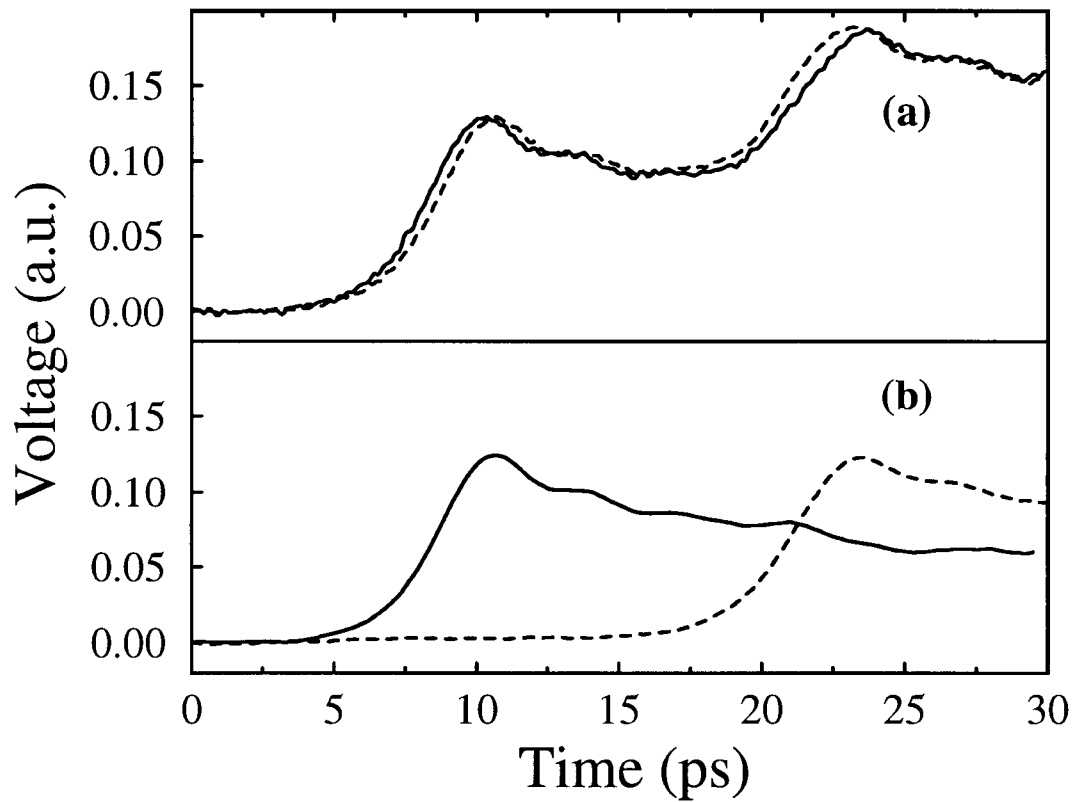


Figure 2.3: Results for open-circuit device:(a) Waveforms measured at locations A (solid line) and B (dashed line) as shown in Fig. 2.2. (b) Recovered incident (solid line) and reflected (dashed line) signals.

percent risetime of the recovered incident signal is 3.7 ps which is very close to the 3.8 ps risetime of the original incident component in the measured results. In this case, since the risetime and amplitudes of the retrieved signals are very close to the unprocessed measurements the choice of distance between the two locations is satisfactory.

It is clear from Fig. 2.3 that the recovered incident and reflected signal are similar to the measured ones. To get a more quantitative measure of similarity we have compared the measured waveforms with the waveforms reconstructed from the recovered incident and reflected signals. In Figs. 2.4(a) and (b) the solid lines show the total signals at locations A and B obtained by summing the recovered incident and reflected signals. The dashed lines in Figs. 2.4(a) and (b) show the difference between the reconstructed waveforms of Fig. 2.4 and the measured waveforms from Fig. 2.3(a); the difference is very small, showing that the recovered signals are in excellent agreement with the measurements. The ratio of the rms value of the error waveforms shown with dashed lines in Fig. 2.4 and the rms value of the measured waveforms in Fig. 2.3(a) at locations A and B are 0.012 percent and 0.016 percent, respectively.

The above results show that overlapping incident and reflected signals can be recovered from measured waveforms by processing in the time-domain and the recovered waveforms agree with the measured results. This is the first demonstration of an approach to achieve extraction of step-like signals when measurements are performed close to the device.

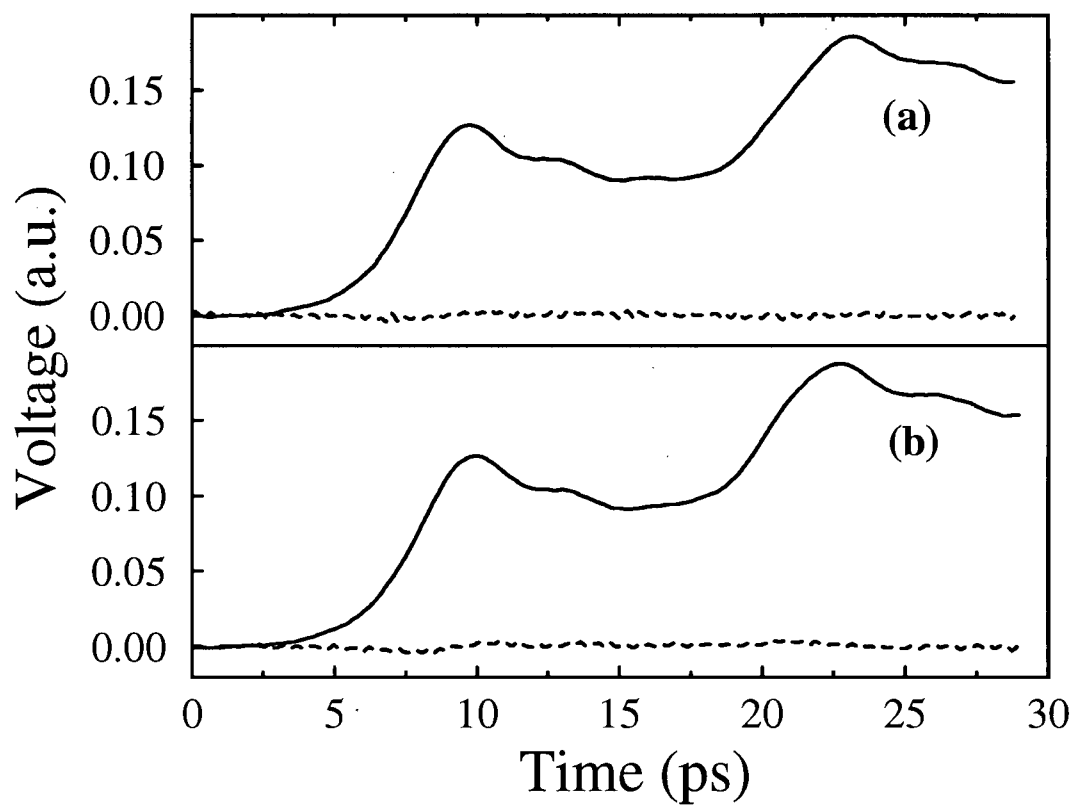


Figure 2.4: Total signals at locations A and B reconstructed from the recovered signals are shown with the solid lines in panels (a) and (b), respectively. The difference between the reconstructed signals and the actual measurements are shown as dashed lines in panels (a) and (b), respectively.

2.3 Fourier-Transform Approach

2.3.1 Theory

The time-domain approach presented in the previous Section has the advantage that the processing is easily applicable to any incident or reflected signals; the limitation is that the measurement locations must be closely spaced to give adequate measurement bandwidth, so that no significant dispersion or attenuation occurs between the two locations. In the following we outline a more general approach that accounts for dispersion and attenuation, and allows arbitrarily large separation between measurement locations; this approach can only be applied to measured signals that can be Fourier transformed. It is interesting to note that the time-domain microwave simulation techniques like Transmission-Line Matrix (TLM) and finite-difference time-domain (FDTD) methods also faces a similar problem when calculations of scattering parameters for a port are required. Thus, numerical processing methods similar to our Fourier-transform approach are used during simulations to calculate the scattering parameters [32].

We outline the Fourier-transform approach by using a hypothetical example to demonstrate that the Fourier-transform approach works remarkably well in the ideal case and to emphasize the usefulness of this approach for S-parameter measurements of a device. To illustrate the technique, suppose that the photoconductive switch generates a pulse as shown in Fig. 2.5(a). A hypothetical reflected pulse from the DUT that is broader and smaller compared to the incident pulse is shown in Fig. 2.5(b). As in the previous Section we assume the signals measured at the two locations A and B have incident and reflected components. The measured signal $g_A(t)$ at location A as shown in Fig. 2.5(c) with solid line can be expressed as in equation (2.1) of the previous Section. The signal measured at location B is

$$g_B(t) = h_{inc}(t) + h_{ref}(t) \quad (2.7)$$

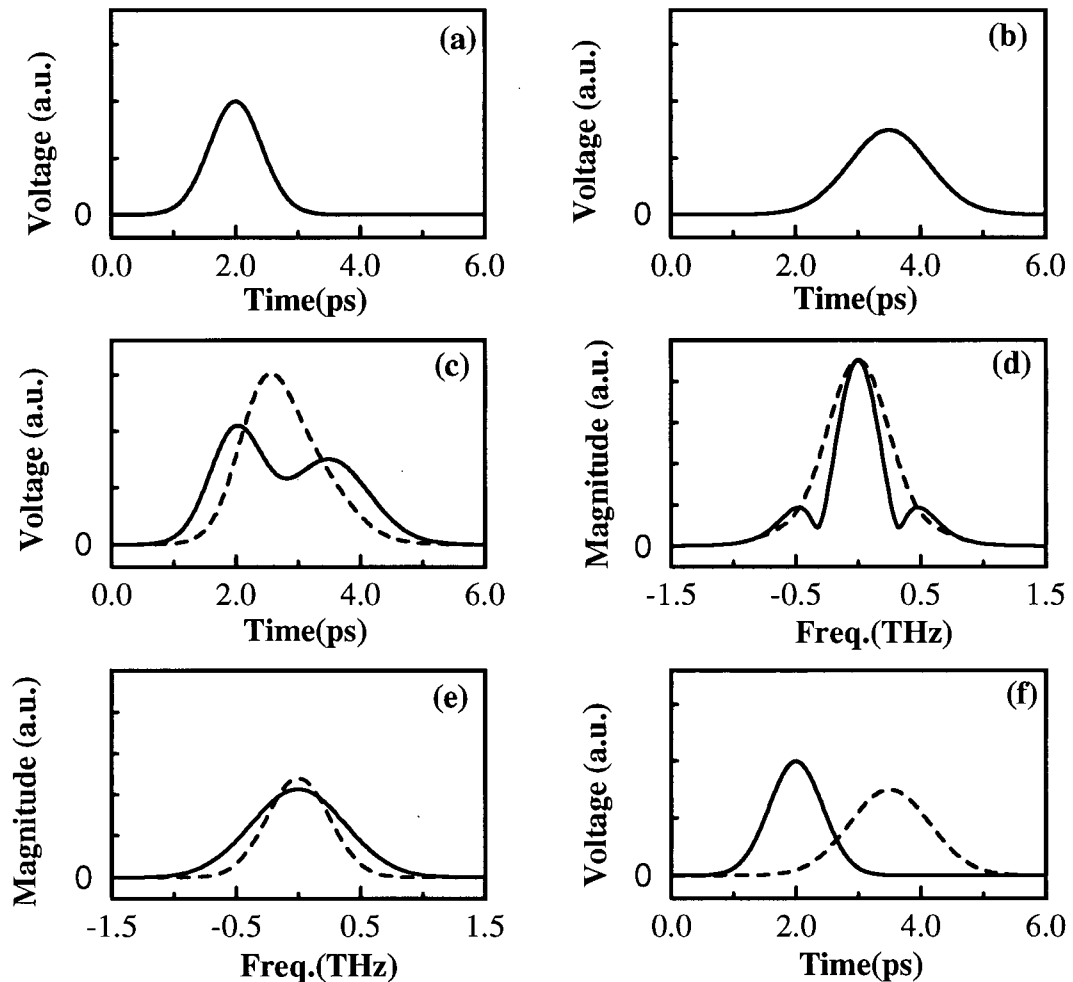


Figure 2.5: *Hypothetical* example illustrating the technique to separate signals using Fourier-transform approach: (a) Incident signal at location A. (b) Reflected signal from the device under test at location A. (c) Waveforms measured at locations A (solid line) and B (dashed line), where location B is closer to the device. (d) Magnitude spectrum of waveforms measured at location A (solid line) and location B (dashed line). (e) Magnitude spectrum of recovered incident signal (solid line) and reflected signal (dashed line) obtained by method outlined in the text. (f) Recovered incident signal (solid line) and reflected signal (dashed line).

where the incident and reflected components, $h_{inc}(t)$ and $h_{ref}(t)$, differ from those measured at location A because of time-delay, dispersion and attenuation. In our hypothetical example we have assumed that there is no dispersion and attenuation between two locations. Thus, the dashed line in Fig. 2.5(c) shows the signal $g_B(t)$ that would be measured at location B which is a superposition of time-delayed incident and time-advanced reflected signals. The Fourier transform of equations (2.1) and (2.7) shows that

$$G_A(\omega) = F_{inc}(\omega) + F_{ref}(\omega) \quad (2.8)$$

$$G_B(\omega) = F_{inc}(\omega)T(\omega, L) + F_{ref}(\omega)T^{-1}(\omega, L) \quad (2.9)$$

where $T(\omega, L)$ describes the transmission of a signal traveling on a transmission line of length L ; it is given by

$$T(\omega, L) = e^{-\gamma(\omega)L}. \quad (2.10)$$

The complex, frequency-dependent propagation constant γ describes attenuation and dispersion characteristics of the transmission line; in the following we assume that it is known as a function of frequency as determined by measurements such as those given in Ref. [9]. If the attenuation and dispersion are negligible over the separation L , then $T(\omega, L)$ describes a simple phase shift between the two measured signals. This phase shift is equivalent to a time shift of the signal in the time domain. In Fig. 2.5(d) we show the magnitude spectra of the waveforms shown in Fig. 2.5(c) to demonstrate that the Fourier-transform of the measured signals can be significantly different from those of the recovered signals.

We can extract incident and reflected signals as a function of frequency from the spectra shown in Fig. 2.5(d) as follows. The incident and reflected signals can be obtained from equations (2.8), and (2.9) as

$$F_{inc}(\omega) = \frac{G_A(\omega)T^{-1}(\omega, L) - G_B(\omega)}{T^{-1}(\omega, L) - T(\omega, L)} \quad (2.11)$$

and

$$F_{ref}(\omega) = \frac{G_B(\omega) - T(\omega, L) G_A(\omega)}{T^{-1}(\omega, L) - T(\omega, L)} \quad (2.12)$$

The magnitude spectra of the recovered incident and reflected signals in this hypothetical example are shown in Fig. 2.5(e) with solid and dashed lines, respectively. As expected the magnitude spectra of the recovered signals are Gaussian since the hypothetical measured signals in the time domain are Gaussian. One can obtain the reflection coefficient as a function of a frequency for our hypothetical device just by taking the ratio of the extracted reflected and incident signals. The recovered signals transformed to the time domain using the inverse Fourier transform are shown in Fig. 2.5(f). The recovered signals are identical to the incident and reflected signals plotted in Fig. 2.5(a) and (b), which were used to construct the hypothetical measured signals $g_A(t)$ and $g_B(t)$.

In summary, the approach presented in this Section has advantages compared to the time-domain approach if the measured signals can be Fourier transformed, because it eliminates the finite-difference approximation required in the time-domain approach. This allows signal recovery for arbitrary separation without bandwidth limitation. The above method can be further extended in the case when attenuation and dispersion characteristics of the line are not known by performing measurements at three separate locations instead of two. Details of this are beyond the scope of the present work.

2.3.2 Experimental Verification

Experimental Arrangement

The short-circuit DUT shown in Fig. 2.6 was photolithographically defined on a 425 μm thick semi-insulating GaAs substrate; the pattern was defined by evaporation of 10nm/200nm thick Ti/Au followed by lift-off. During the experiment, we used the non-contact configuration with an air gap between electro-optic transducer and transmission

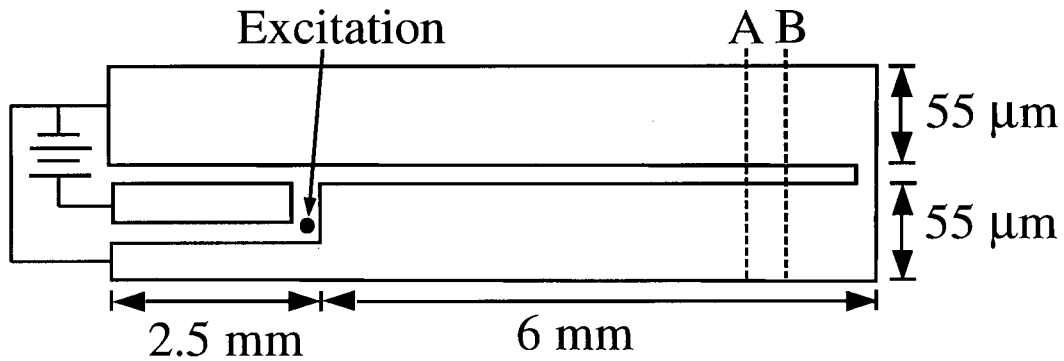


Figure 2.6: Layout of coplanar stripline test-structure with short-circuit device, and a photoconductive generator. All gaps are $5 \mu\text{m}$.

line of approximately $5 \mu\text{m}$ for all measurements. The other experimental details are identical to those described in Section 2.2.2.

Results

In Fig. 2.7 we show the data measured for the short-circuit sample described above, and the recovered incident and reflected signals. The solid line of Fig. 2.7(a) shows the signal $g_A(t)$ measured at location A of Fig. 2.6, located $600 \mu\text{m}$ from the short-circuit DUT. The step-like incident signal $f_{inc}(t)$ is followed by a negative-going step-like reflection $f_{ref}(t)$ starting at approximately 17 ps. The dashed line in Fig. 2.7(a) shows the signal $g_B(t)$ measured at location B, which is $50 \mu\text{m}$ closer to the short circuit than A. The measured signals $g_A(t)$ and $g_B(t)$ approach zero at approximately 30 ps. The sampling period was chosen to be 167 fs. For numerical processing, the measured waveforms were interpolated by four points between each of the measured data points.

To perform the Fourier transform, we assumed that the measured signals remain at zero after 30 ps. This assumption is not exact but it works nicely for our demonstration. The magnitude spectra of the measured signals at locations A and B are shown in

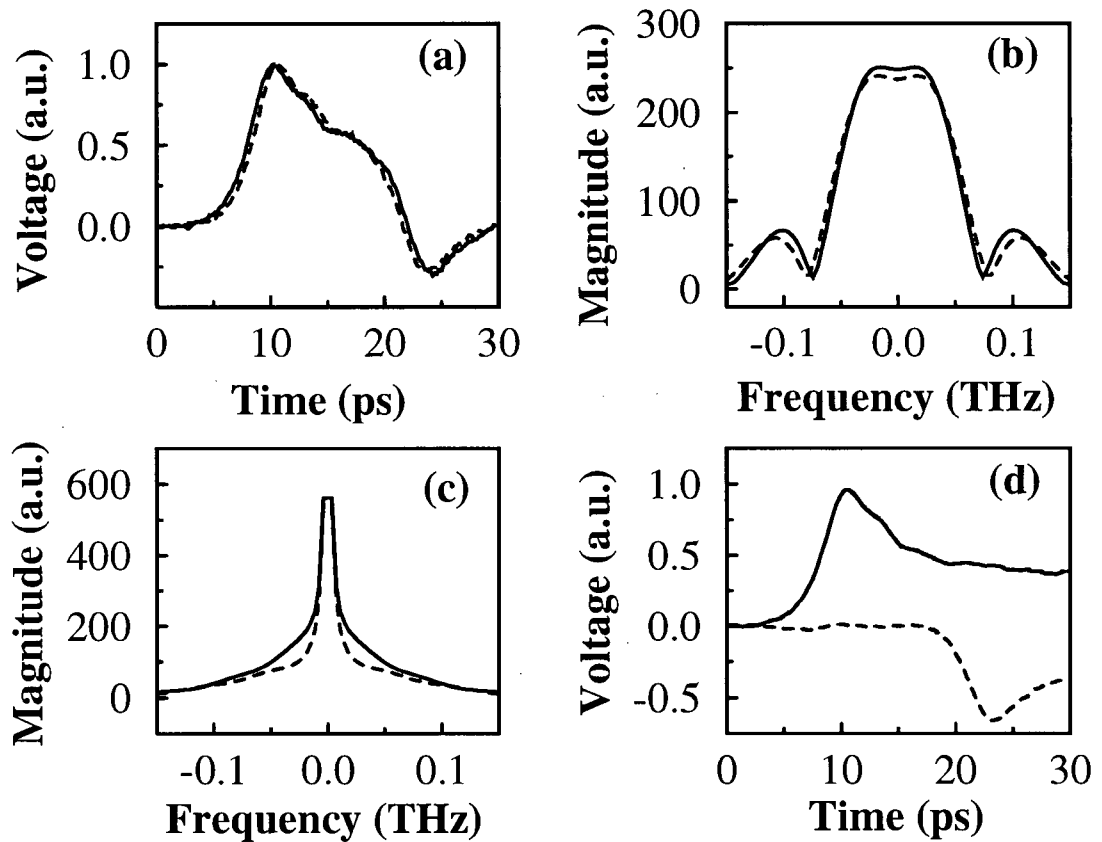


Figure 2.7: Results for short-circuit device: (a) waveforms measured at locations A (solid line) and B (dashed line) of Fig. 2.6; (b) magnitude spectra of the measured waveforms; (c) magnitude spectra of recovered incident (solid line) and reflected (dashed line) signals; (d) recovered incident (solid line) and reflected (dashed line) waveforms.

Fig. 2.7(b) as solid and dashed lines, respectively. The magnitude spectra look quite similar as expected from the time-domain signals. However, the second peak in the spectra is slightly shifted towards high-frequency in the dashed line curve corresponding to location B; this is to be expected since the delay between the positive-going incident signal and the negative-going reflected signal is less in the measured signal. Since the measurement separation of $50\ \mu\text{m}$ is small, we have assumed that dispersion and attenuation are negligible. The constant propagation velocity v was determined by measurement. The magnitude spectra of the recovered incident and reflected signals are shown in Fig. 2.7(c) as solid and dashed lines, respectively. The magnitude spectra of the recovered signals are quite different; the recovered reflected signal clearly show loss of energy approximately between 10 GHz and 100 GHz. The time-domain recovered waveforms are plotted in Fig. 2.7(d), where the solid line shows the incident signal, and the dashed line the reflection.

Discussion

The recovered incident signal plotted with solid line in Fig. 2.7(d) shows step-like signal with maximum amplitude close to that seen in the measured signals in Fig. 2.7(a). The features in the recovered incident signal between 10 to 15 ps are similar to the measured signals. It is interesting to note that the reflected signal amplitude is significantly smaller than the incident signal, indicating that reflection from the short circuit is lossy in the frequency range considered here. In general, the recovered signal is a negative-going step-like signal as expected from a short-circuit. The amplitude of both recovered signals at 30 ps are the same with opposite signs to make overall signal zero as assumed. The 10 to 90 percent risetime of the recovered incident signal is 3.9 ps which is similar to those of the measured signals further proving that the Fourier-transform approach is not bandwidth limited. Here we have demonstrated that it is not necessary to have pulse-like individual incident and reflected signals to use the Fourier-transform approach; the

approach works equally well with the incident and reflected signals of any shape provided measured signals can be Fourier-transformed.

Finally, we compare the Fourier-transform method demonstrated in this Section to the time-domain approach. The time-domain approach of Section 2.2.1 was used to recover the incident and reflected signals from the data of Fig. 2.7(a) for the short-circuit device; the results are shown as the dashed lines in Figs. 2.8(a) and (b). For comparison, the solid lines in Figs. 2.8(a) and (b) show signals obtained by processing in the frequency domain. The features in the recovered signals using both techniques are quite similar. The discrepancy can be attributed to the slight difference in the propagation velocity used in the two approaches. The non-zero component in the recovered reflected signal at approximately 7 ps can be attributed to the fluctuations in laser power during the measurement, as will be discussed in the following Section.

In summary, we have demonstrated that one can recover overlapping signals by processing in the frequency domain. The recovered waveforms using the Fourier-transform approach are quite similar to the ones obtained by performing calculations in the time domain.

2.4 Experimental Considerations

There are several experimental factors that play a significant role in determining the success of the two techniques described in the previous Sections. As described by equations (2.4), (2.3), (2.11), and (2.12) both methods rely on cancelling the incident component to determine the reflected signal and vice versa. Thus, it is essential to have identical conditions when signals are measured at two separate locations. The critical experimental factor is the drift in the laser power over time. Typically about 6 to 7 signals were averaged to obtain the waveforms shown in this Chapter. It took an average of 10 minutes

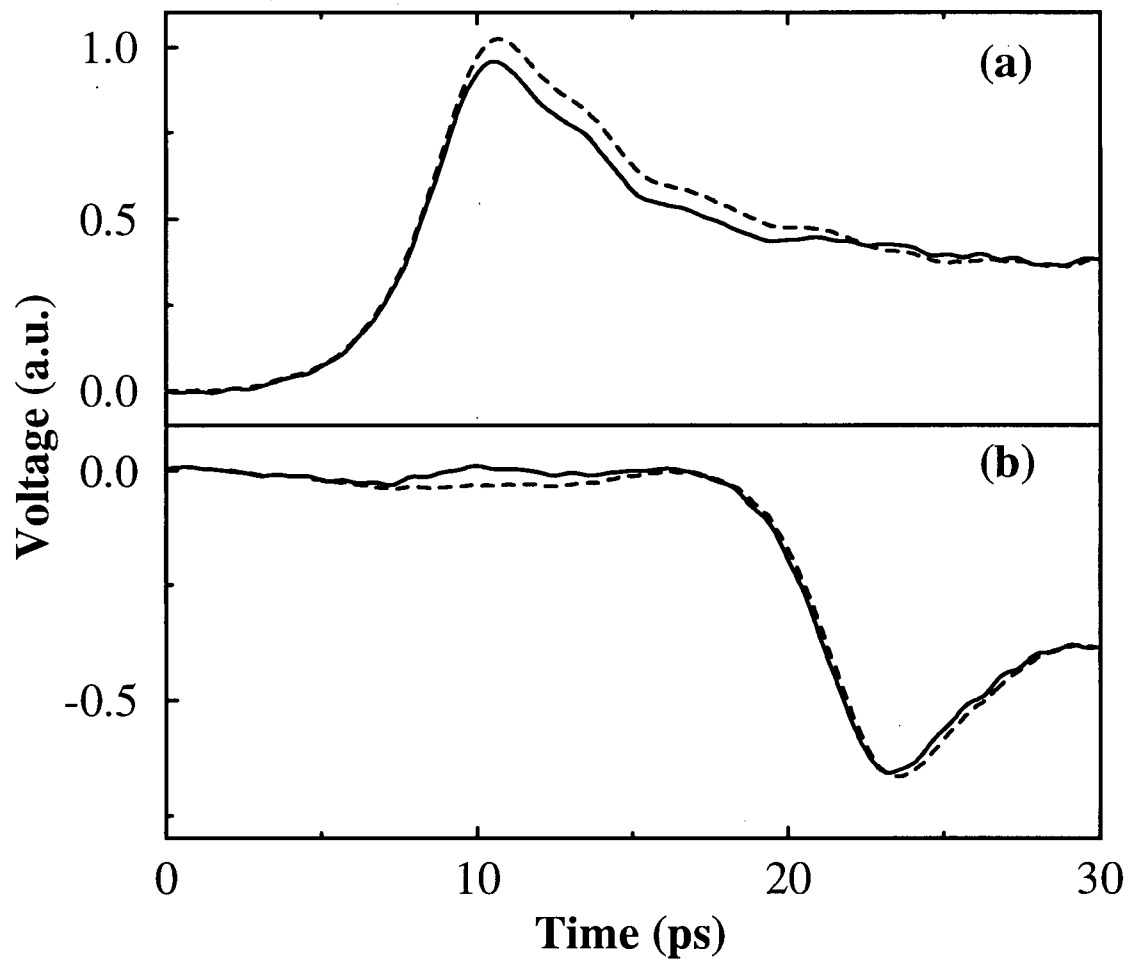


Figure 2.8: Comparison of results for short-circuit device: (a) incident signal; (b) reflected signal. In both panels the dashed line shows results obtained by time-domain processing, and the solid line by frequency-domain processing.

to do a single scan, so the laser power and alignment have to be steady for about two hours to have identical measurement conditions. Any drift in the laser power can show up as features in the recovered signals that are not present in both measured signals. Furthermore, changes in laser alignment or power in general do not have a linear effect on the excited signals that can be easily corrected since the photoconductive switch is a non-linear device with respect to pump power and pump beam location.

The second critical factor is the alignment of the LiTaO_3 transducer during change in measurement locations. One cannot move the probe-beam inside the transducer to have change in measurement locations since the measured signal inside the transducer can be location dependent [30, 31]. Thus, it is essential to move either the transducer and the probe beam, or the sample holder and the excitation beam. During this translation it is necessary to have constant air-gap between the transducer and the sample as well as to have identical sampling location for probe-beam on the transmission line. During change in the measurement location, it is also essential to have identical excitation locations since the excitation location has a large effect on the shape and amplitude of the waveform generated.

It is clear from equations (2.11)- (2.12) that the accuracy of the results for the Fourier-transform approach depend on the accuracy of the translation stage used during change in measurement locations. In summary, there are several experimental factors that will determine accuracy of the recovered results and success of the above techniques. These weaknesses can be overcome by carefully designing and conducting the experiment.

2.5 Conclusions

We have proposed and demonstrated a new technique, based on electro-optic sampling at two different locations, to resolve superimposed incident and reflected signals propagating in opposite directions. If the two locations are close to one another, the incident and reflected signals can be separated unambiguously using simple time-domain processing. To allow high-bandwidth signal recovery, the two sampling locations must be separated by a small distance. We have also extended this approach for signals that can be Fourier transformed, and accounted for dispersion and attenuation between the sampling locations using processing in the frequency domain. This Fourier-transform approach has the advantage that there is no bandwidth limitation for any separation of measurement locations. Finally, we note that the technique we have described can be applied to any time-resolved sampling technique including photoconductive sampling.

Chapter 3

Guided Substrate Waves Generated by Photoconductive Excitation

3.1 Introduction

3.1.1 Background and Motivation

As briefly described in Chapter 1, electro-optic and photoconductive sampling employ a photoconductive switch to generate fast electrical signals on the transmission line. The photoconductive switch is also capable of generating THz bandwidth signals which could propagate in the substrate. The first observation of a feature generated by the photoconductive switch and attributed to a reflection from the back surface of the substrate was observed by photoconductive sampling on the coplanar transmission line [25]. The dotted line in Fig. 3.1 shows the photoconductively-sampled waveform from Ref. [25]. The feature represented by the first positive-valued peak to the right of the main peak is due to a reflection from the backside of the substrate. The authors of Ref. [25] have observed a direct correlation between the relative arrival time of the substrate reflection with respect to the main peak and the substrate thickness. They have completely removed the observed back side reflection from the sampled waveforms and also decreased the amplitude of the shoulder by placing a microwave-absorbing material on the back side of the wafer; the waveform showing elimination of the back side reflection is plotted with the solid line in Fig. 3.1.

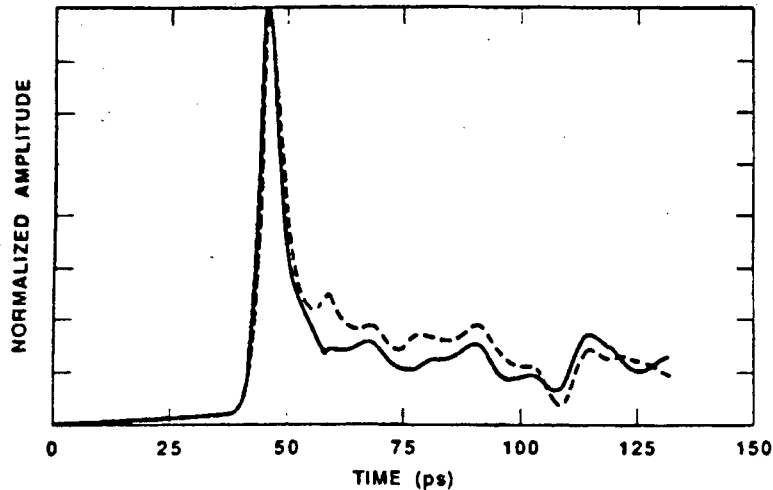


Figure 3.1: Sampled waveform showing the back plane reflection. The dotted line shows a waveform exhibiting a reflection from the back side of the substrate as manifested by the first positive-valued peak to the right of the main peak. The solid line represents the sampled data acquired from a transmission line when a microwave-absorbing material was placed under the GaAs wafer (from Ref. [25]).

In Fig. 1.9(c) of Chapter 1 and replotted in Fig. 3.2, we have also seen a feature at approximately 17 ps that cannot be correlated with any physical spacing of the transmission line discontinuities. The feature arrives at a sampling location remote from the photoconductive generator at a time later than the signal travelling on the transmission line; we will refer to this feature as the THz signal. In order to identify the path travelled by this THz signal we need to perform measurements on similar coplanar structure fabricated on semi-insulating GaAs with various substrate thicknesses. Furthermore, it is essential to determine the propagation properties of this THz signal. If the signal is guided by the transmission line as part of the coplanar stripline mode then this wide-bandwidth signal can be used to characterize devices. However, if the signal is not part of the coplanar stripline mode the device may not respond to this wide-bandwidth signal and it will interfere with device characterization.

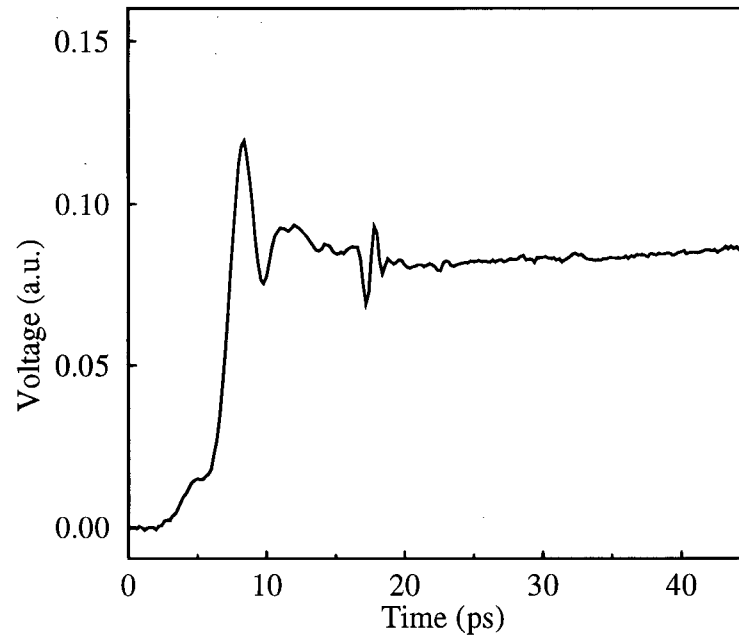


Figure 3.2: Electro-optic measurement showing the THz feature at approximately 17 ps generated by the photoconductive switch. The sampling was performed on the LT GaAs sample approximately 1.5 mm away from the photoconductive switch.

3.1.2 Summary of Results

We show clear observations of a THz signal generated by the photoconductive switch and measured on the transmission line. The arrival time is related to the thickness of the substrate. By making measurements on the transmission line (on-axis) and far away from the transmission line (off-axis) we are able to clearly show that the THz feature is due to electromagnetic waves traveling in the substrate. In addition, the electro-optic technique provides a unique probe of the properties of these substrate waves: we find that they are trapped beneath the metallic electrodes in samples with thin substrates. Finally, we have been able to eliminate this substrate-wave signal by effectively increasing the thickness of the substrate; this delays the signal sufficiently that it arrives outside the time window of interest.

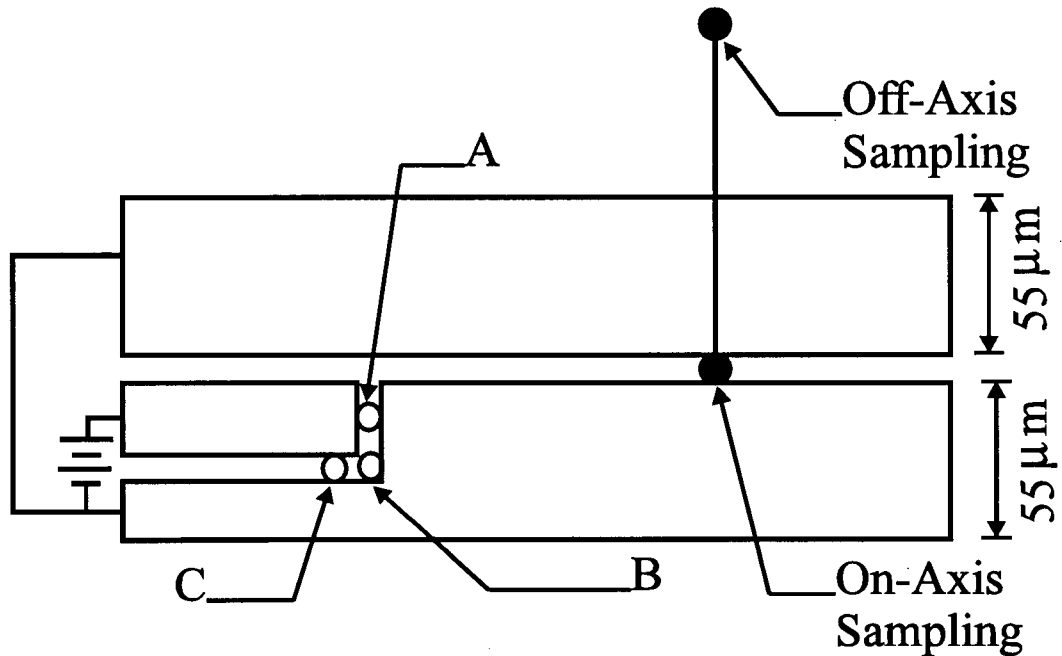


Figure 3.3: Layout of coplanar stripline with a photoconductive generator (not to scale). All gaps are $5\ \mu\text{m}$, and locations A, B, and C are the excitation positions referred to in the text.

3.1.3 Outline of Chapter

In Section 3.2 we describe the experimental arrangement and sample preparation. The electro-optic sampling measurements for samples with different thicknesses are presented in Section 3.3. These results are discussed in Section 3.4. Finally, in Section 3.5 we have summarized our conclusions.

3.2 Experiment

The coplanar stripline (CPS) shown in Fig. 3.3 is photolithographically defined on semi-insulating GaAs substrates of varying thicknesses: 500 and 650 μm . The metallization on 650 μm thick samples are defined by evaporation of 10nm/200nm thick Ti/Au followed by lift-off. Excitation is at one of locations A, B and C; dimensions are shown in Fig. 3.3.

While many measurements using external LiTaO_3 sampling tips have been made with the tip in direct contact with the transmission line, it has recently been shown that the impedance mismatch due to the LiTaO_3 tip can cause significant distortions of the measured results [30, 31]. Therefore, we use a non-contact probing configuration with an air gap between electro-optic transducer and transmission line to reduce the distortions of the measured results. In addition to measurements on the axis of the transmission line, we also make measurements with the probe tip laterally displaced from the center by varying distances; we will refer to the two types of measurements as on- and off-axis, respectively. A switch bias of 7.5V was used in all measurements.

3.3 Results

Initial measurements of the THz signal were performed on samples with substrate thicknesses of 650 μm and 500 μm . The sampling locations for these on-axis measurements are approximately 1.5 mm away from the photoconductive switch and excitation is at position A of Fig. 3.3. In Fig. 3.4 the solid and dashed lines show signals measured on the 650 and 500 μm thick samples, respectively. We have time-shifted the two signals so that the leading edges coincide to facilitate direct comparison of the relative arrival times of the THz signals. The arrows in Fig. 3.4 indicate the THz feature in each measurement. It is clear from Fig. 3.4 that the relative arrival time of the THz signal varies with substrate thickness, indicating it travels in the substrate.

To further study the properties of the THz signal, we prepared a new set of samples with a wider range of substrate thicknesses. In addition, in these samples we perform on- and off-axis measurements. In Fig. 3.5(a) the solid line shows the signal measured on-axis for a sample with substrate thickness of 650 μm . The sampling location for this case is approximately 1.67 mm from the photoconductive switch, and excitation is at

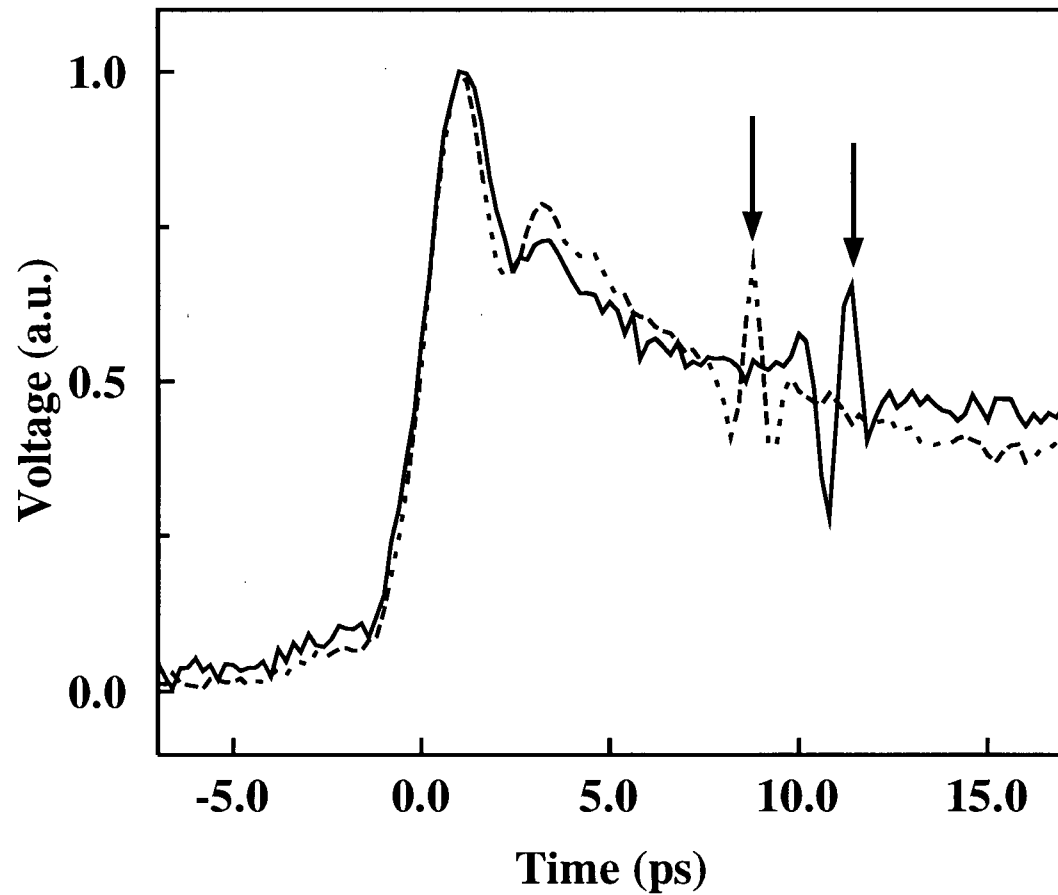


Figure 3.4: Electro-optic sampling measurements performed approximately 1.5 mm away from the photoconductive switch: the solid and dashed lines show measurements for 650 μm thick and 500 μm thick samples, respectively. The arrows indicate the THz feature in each waveform.

position A of Fig. 3.3. As expected with the long-lifetime semi-insulating substrate, the generated signal is step-like. However, at approximately 16 ps a new feature is seen with a number of oscillations with a period of approximately 1.5 ps. Both the THz feature and the step signal disappear with zero bias and changes its sign when negative bias voltage is applied to the photoconductive switch verifying that both features are generated by the photoconductive excitation at the switch. Because generation of THz radiation is related to the separation of charges that occurs after photoconductive excitation, one might expect the oscillatory feature we see to depend upon the direction of the charge separation with respect to the measurement position. We checked this by excitation at the three locations A, B, and C of Fig. 3.3. At all three positions we observe similar THz signals, indicating that the orientation responsible for generation of the feature we see is perpendicular to the metal-semiconductor interface.

To further characterize the THz signal, we make measurements off-axis at a distance 350 μm from the center of the transmission lines. With our electrode width of 55 μm we would expect to detect only a small signal from the fringing field of the radiation propagating in the fundamental CPS mode; any observed signal should be related to the evanescent field of any substrate modes that are excited. We have verified that the leakage of field from the transmission lines into the transducer during off-axis probing is small by comparing the electro-optic signals measured on and off-axis when a DC calibration signal is applied to the transmission line. In Fig. 3.5(a) we show the off-axis measurement as a dashed line. The main feature observed in the off-axis curve is an oscillatory feature starting at approximately 16 ps. It is nearly identical in amplitude to the THz feature observed on-axis. We have performed off-axis measurements at other locations with distances up to 500 μm away from the transmission line and similar off-axis waveforms are observed.

To further study the effect of substrate thickness we prepared a sample with 83

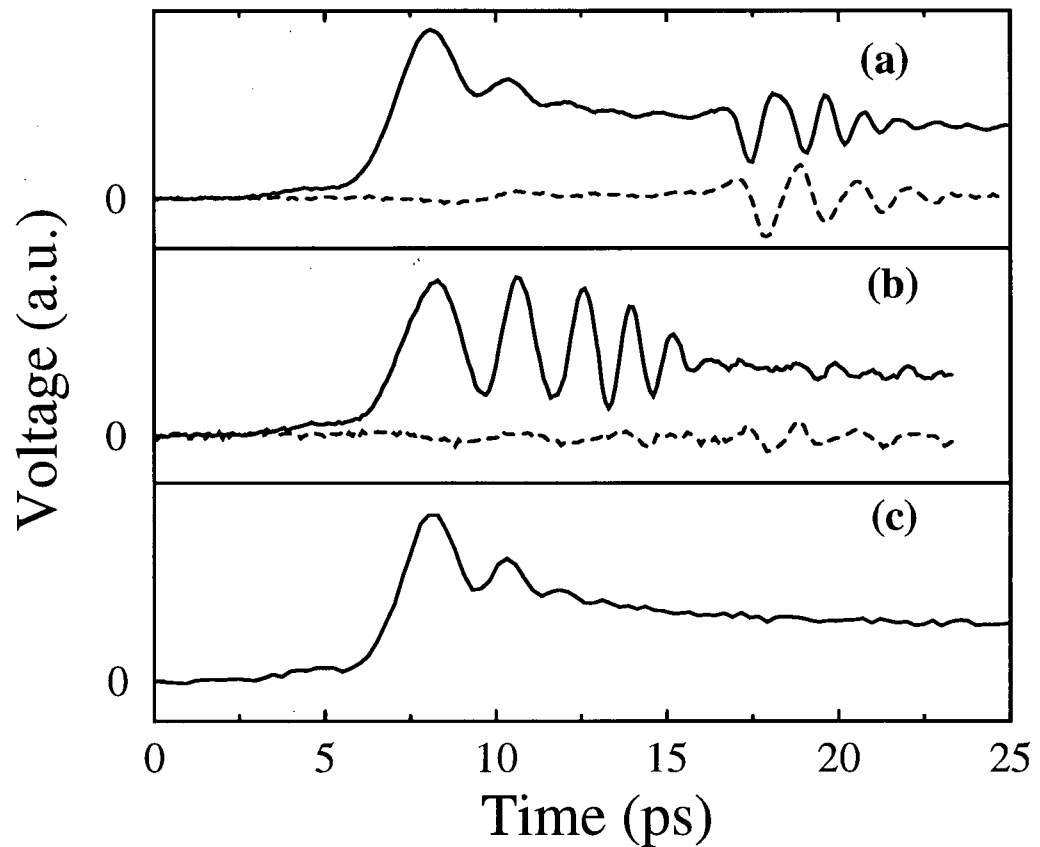


Figure 3.5: Measured signals for three substrate thicknesses. (a) On-axis (solid line) and off-axis (dashed line) measurements for a $650 \mu\text{m}$ thick sample. (b) On-axis (solid line) and off-axis (dashed line) measurements for the $83 \mu\text{m}$ thick sample. (c) On-axis measurements for the 1.3 mm thick sample.

μm substrate thickness by mechanical lapping (grinding) of a $650\ \mu\text{m}$ thick substrate. In Fig. 3.5(b) we show the on- and off-axis measurements as the solid and dashed lines, respectively; sampling and excitation conditions are the same as those used for Fig. 3.5(a). Note that to facilitate comparison of the waveforms for different samples, we have time-shifted the curves of Fig. 3.5(b) so that the leading edge of the on-axis signal coincides with the corresponding waveform of Fig. 3.5(a). The on-axis signal has oscillatory features appearing very soon after the initial peak; in addition, the relative amplitude of these features is significantly greater than in the $650\ \mu\text{m}$ sample. The off-axis measurement shows no obvious evidence of a substrate signal in this case; the origin of the smaller features occurring after approximately 15 ps is not known.

Because these THz signals are problematic in device characterization, it is important to be able to eliminate them from the measurements. In Ref. [25] microwave-absorbing material on the backside of the substrate was used to eliminate the backside reflections. An alternative approach is demonstrated in Fig. 3.5(c), where the $650\ \mu\text{m}$ sample being tested is placed on another unpatterned substrate of equal thickness. In this case the sampling location was 1.5 mm from the photoconductive switch. As can be seen in Fig. 3.5(c), only a step-like signal is seen in the time-window shown; the THz signal actually arrives at approximately 31 ps. We see no evidence of a reflection from the interface between the two substrates, which are simply cleaned and held in mechanical contact.

3.4 Analysis

As seen in the curves of Figs. 3.4 and 3.5, the delay between the leading edge of the step-like and the THz signals varies significantly with substrate thickness. A simple estimate of the expected delay can be made if we assume the CPS signal travels with a relative

dielectric constant of $(\epsilon_r + 1)/2$ and the substrate wave travels with the relative dielectric constant of the substrate, ϵ_r . The substrate wave is assumed to be reflected from the backside, and thus travels a distance that can be simply related to the thickness of the substrate and the position of the sampling location. The delay Δt is given by

$$\Delta t = 2 \frac{\sqrt{\epsilon_r}}{c} \sqrt{\left(\frac{z}{2}\right)^2 + h^2} - \frac{z}{c} \sqrt{\frac{\epsilon_r + 1}{2}} \quad (3.1)$$

where z is the distance from the photoconductive switch to the sampling location, and h is the substrate thickness. In Fig. 3.6 we show the delay Δt calculated from Eq. 3.1 for $z=1.5$ and 1.67 mm as a function of GaAs substrate thickness. We have estimated the relative arrival time from the measured waveforms by comparing the delay between the beginning of the step-like, and the THz signals. The delay estimated for waveforms in Fig. 3.4 are plotted in Fig. 3.6(a) with open circles. Fig. 3.6(a) also includes the delay obtained from the measurement on the 1.3 mm thick GaAs. The delay estimated for on-axis waveforms plotted in Figs. 3.5(a) and (b) for $650 \mu\text{m}$ and $83 \mu\text{m}$ thick GaAs substrates are indicated in Fig. 3.6(b). Since it is difficult to determine the beginning of signals the estimated error bars for the delays are also shown in Fig. 3.6. It is clear from Fig. 3.6 that the delay estimated by Eq. 3.1 agrees very well with the relative arrival times observed, confirming our interpretation of the origin of the signal as reflection from the backside of the substrate.

It is interesting to note that the highly-structured THz signals observed are quite different from those reported in Refs. [23] and [25]. This may be due to the limited bandwidth for the photoconductive sampling used in Ref. [25]. A direct comparison with the results of Ref. [23] is difficult because of the difference in the direction of observation, and sample geometry. An explanation for the observed resonance can be found in Ref. [17], where loss on coplanar waveguides (CPW) due to coupling between the CPW mode and surface-wave modes was studied. They predicted that for finite

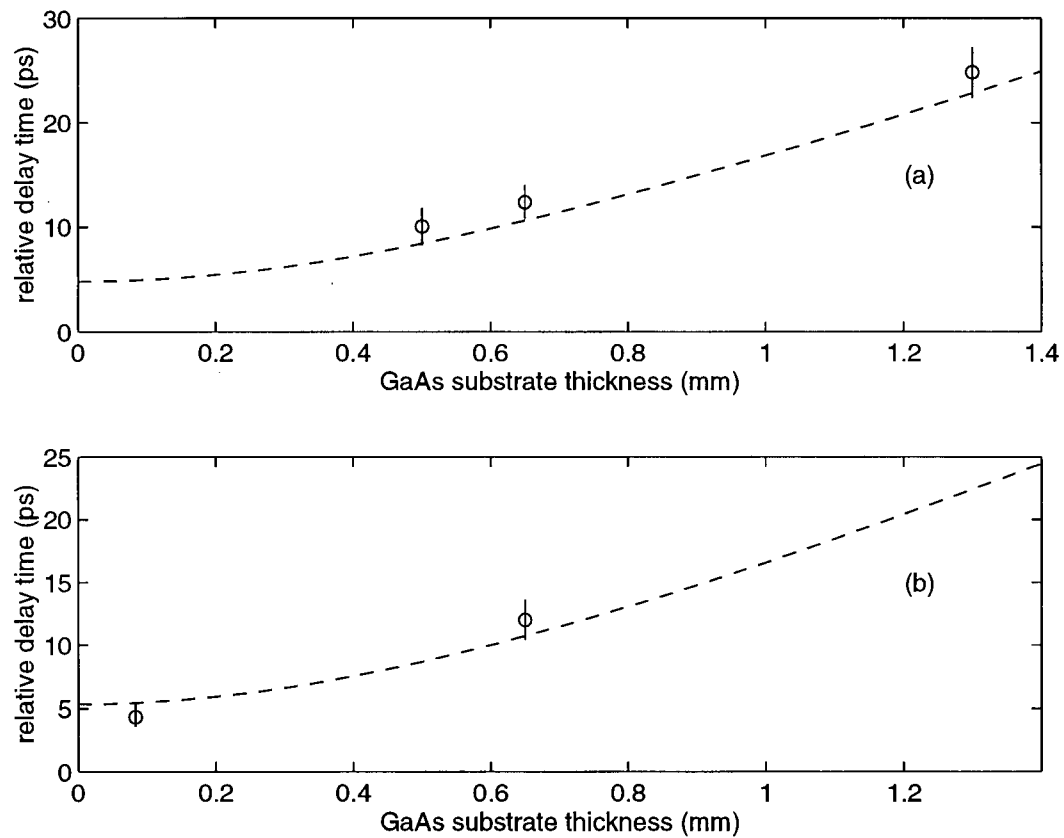


Figure 3.6: Relative delay of the THz signal calculated from Eq. 3.1 for various substrate thicknesses is plotted with the dashed line. The panels (a), and (b) are for distances of 1.5 and 1.67 mm from the photoconductive switch to the sampling location, respectively. The experimental delay from the measured waveforms are plotted with the open circles. The vertical bar through the circle is an error bar for the experimental delay.

ground-electrode widths, resonances would occur in the CPW/surface-wave coupling due to reflections of the surface-wave confined under the electrodes from the outer edges of the ground electrodes. In our situation, such reflections could occur at the outer edges of the two electrodes; the traversal time across the $115 \mu\text{m}$ width of the transmission line by a substrate wave travelling with the dielectric constant of the substrate is approximately 1.4 ps. A recent study of such leakage in coplanar striplines has been reported in Ref. [33]; their study shows no resonances in the CPS mode loss that can be attributed to the resonances seen in the CPW case. However, in using the theoretical studies of surface-wave leakage in the interpretation of our results, it is important to stress the differences between the calculations and our experiments. The calculations show the effect of surface-wave modes on the propagation of the CPS or CPW modes; the properties of surface wave modes are determined mainly by looking at their influence on the fundamental coplanar modes. However, in our case we are directly probing the properties of the substrate modes that we have photoconductively excited, even in situations where they may not have great influence on the fundamental CPS mode. A full calculation of the properties of the surface waves has not been reported, and is beyond the scope of the present work; however, we do not feel that the results of Ref. [33] are in contradiction with our interpretation of the resonance in terms of reflections at the outer edges of the electrodes. We further note that this explanation is consistent with the fact that the oscillation period is not significantly affected by the substrate thickness.

Another surprising feature of the data shown in Fig. 3.5 is that while the substrate-wave features are very pronounced in the thin sample measured on-axis, no signal is seen off-axis. This means that for the thin sample, the radiation is confined in the vicinity of the coplanar electrodes. This effective guiding of the surface-wave modes by the metallic electrodes is consistent with the conclusions of Ref. [33], where it was shown that in addition to the CPS mode, a coplanar stripline can also guide a new surface-wave-like

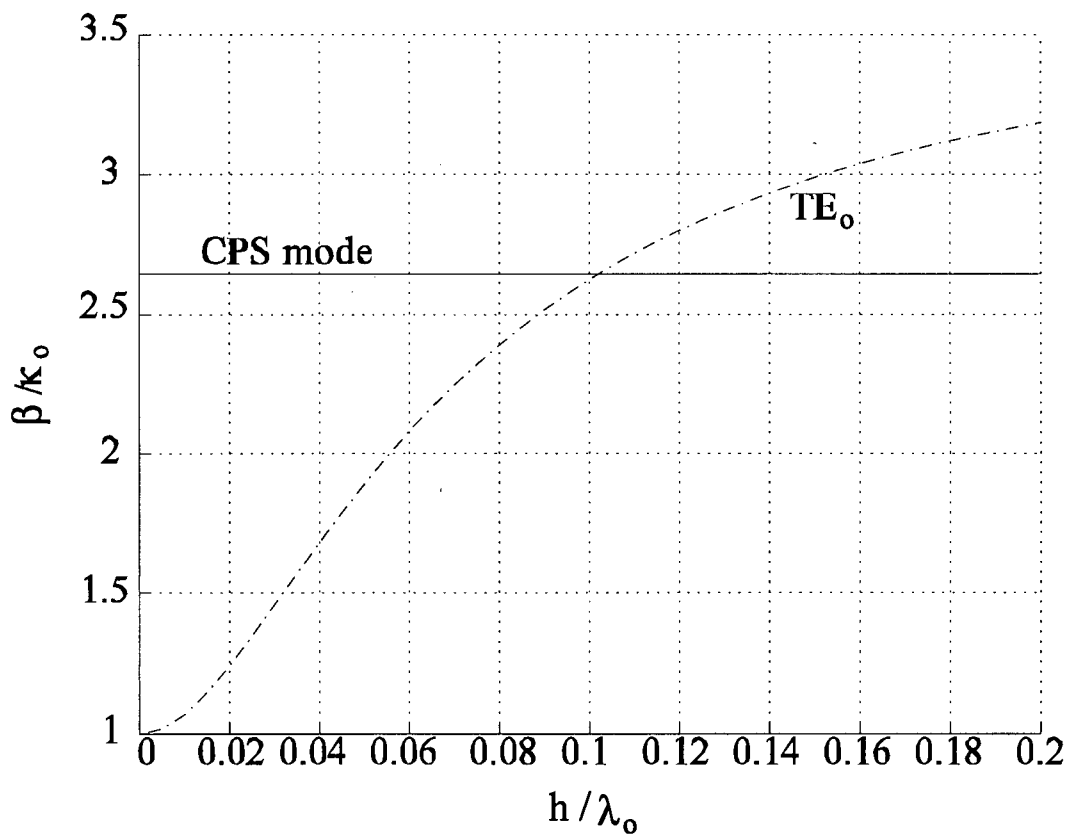


Figure 3.7: Effective dielectric constant for TE₀ mode of GaAs slab is plotted as a function of h/λ_0 using the dashed-dot line. The effective dielectric constant of the CPS mode on a GaAs substrate is plotted with the solid line. The critical h/λ_0 where the new surface-wave-like mode will become leaky can be estimated from the point where two curves cross.

mode for thin substrates. The new surface-wave mode has a field distribution similar to that of the TE_0 mode of the surrounding dielectric. Lin [33] also pointed out that in thick substrates this new mode evolves into a complex leaky mode with power coupling into the TE_0 mode, similar to what is seen in Ref. [17] for the CPW case. In Fig. 3.7 we show the dispersion curve of the TE_0 mode for the GaAs substrate. We have also plotted the quasi-static effective dielectric constant ϵ_{eff} of the CPS mode on GaAs. According to Ref. [33], a guided surface-wave-like mode can be supported for substrates thinner than a critical thickness where the effective dielectric constants of the CPS mode and the TE_0 mode of the surrounding dielectric slab are equal. From Fig. 3.7 we can estimate that this occurs at $h/\lambda_0=0.1$. For our case, where the period of the THz signal is approximately 1.5 ps, or $\lambda_0=450 \mu\text{m}$, the critical substrate thickness is thus approximately $50 \mu\text{m}$. Therefore we expect the substrate waves in the $650 \mu\text{m}$ sample to be quite leaky, and those in the $83 \mu\text{m}$ sample to be much closer to being perfectly guided.

3.5 Conclusions

We have shown that new features appearing in electro-optic measurement of photo-conductively-generated signals on coplanar striplines can be attributed to substrate waves. The arrival time of the THz feature is related to the thickness of the substrate. Measurements on and off the axis of the transmission line show that for thin substrates the substrate waves are effectively guided by the presence of the coplanar stripline electrodes, in agreement with recent work by Tsuji *et. al.* [17] and Lin and coworkers [33].

Bibliography

- [1] L. D. Nguyen, A. S. Brown, M. A. Thompson, and L. M. Jelloian, "50-nm self-aligned-gate pseudomorphic AlInAs/GaInAs high electron mobility transistors," *IEEE Transactions on Electron Devices*, vol. 39, pp. 2007–2014, September 1992.
- [2] P. Ho, M. Y. Kao, P. Chao, K. H. Duh, J. M. Bllingall, S. T. Allen, A. J. Tessmer, and P. M. Smith, "Extremely high gain 0.15 μm gate-length InAlAs/InGaAs/InP HEMTs," *Electronics Lett.*, vol. 27, pp. 325–327, February 1991.
- [3] J. A. Valdmanis, G. Mourou, and C. W. Gabel, "Picosecond electro-optic sampling system," *Applied Physics Lett.*, vol. 41, pp. 211–212, 1982.
- [4] J. A. Valdmanis, "Electro-optic measurement techniques for picosecond materials, devices, and integrated circuits," in *Measurement of High Speed Signals in Solid State Devices* (R. B. Marcus, ed.), San Diego: Academic Press, 1990.
- [5] D. H. Auston, "Picosecond optoelectronic switching and gating in silicon," *Applied Physics Lett.*, vol. 26, pp. 101–103, January 1975.
- [6] D. H. Auston, "Picosecond photoconductivity: High-speed measurements of devices and materials," in *Measurement of High Speed Signals in Solid State Devices* (R. B. Marcus, ed.), San Diego: Academic Press, 1990.
- [7] M. Y. Frankel, J. F. Whitaker, and G. A. Mourou, "Optoelectronic transient characterization of ultrafast devices," *IEEE J. Quantum Electron.*, vol. 28, pp. 2313–2324, October 1991.
- [8] A. Zeng, M. K. Jackson, M. Van Hove, and W. De Raedt, "On-wafer characterization of $\text{In}_{0.52}\text{Al}_{0.48}\text{As}/\text{In}_{0.53}\text{Ga}_{0.47}\text{As}$ modulation-doped field effect transistor with 4.2 ps switching time and 3.2 ps delay," *Applied Physics Lett.*, vol. 67, pp. 262–263, July 1995.
- [9] M. Y. Frankel, S. Gupta, J. Valdmanis, and G. Mourou, "Terahertz attenuation and dispersion characteristics of coplanar transmission lines," *IEEE Transactions on Microwave Theory and Techniques*, vol. 39, pp. 910–916, June 1991.
- [10] S. Alexandrou, R. Sobolewski, H. Nakano, B. Tousley, and T. Y. Hsing, "Picosecond characterization of bent coplanar waveguide," *IEEE Microwave and Guided Wave Lett.*, vol. 1, pp. 231–238, September 1991.

- [11] M. Y. Frankel, R. H. Voelker, and J. N. Hilfiker, "Coplanar transmission lines on thin substrates for high-speed low-loss propagation," *IEEE Transactions on Microwave Theory and Techniques*, vol. 42, pp. 396–402, March 1994.
- [12] C. P. Wen, "Coplanar waveguide: A surface strip transmission line suitable for nonreciprocal gyromagnetic device applications," *IEEE Transactions on Microwave Theory and Techniques*, vol. 17, pp. 1087–1090, December 1969.
- [13] K. C. Gupta, R. Garg, and I. J. Bahl, *Microstrip Lines and Slotlines*. New York: Artech House, 1979.
- [14] E. M. Godshack, "Generation and observation of surface wave on dielectric slabs and coplanar structures," in *1993 IEEE Microwave Theory Tech. Symp. Dig.*, pp. 923–926, 1993.
- [15] D. P. Kasilingam and D. B. Rutledge, "Surface-wave losses of coplanar transmission lines," in *1993 IEEE Microwave Theory Tech. Symp. Dig.*, pp. 113–116, 1983.
- [16] I.-J. F. M. Riaziat, R. Majid-Ahy, "Propagation of modes and dispersion characteristics of coplanar waveguides," *IEEE Transactions on Microwave Theory and Techniques*, vol. 38, pp. 245–251, March 1990.
- [17] M. Tsuji, H. Shigesawa, and A. A. Oliner, "New interesting leakage behavior on coplanar waveguide of finite and infinite widths," *IEEE Transactions on Microwave Theory and Techniques*, vol. 39, pp. 2130–2137, December 1991.
- [18] S. Alexandrou, C.-C. Wang, M. Currie, R. Sobolewski, and T. Y. Hsiang, "Loss and dispersion at subterahertz frequencies in coplanar waveguides with varying ground-plane widths," in *Technologies for Optical Fiber Communications, Proceedings of SPIE*, vol. 2149, pp. 108–118, 1994.
- [19] A. Zeng, *Characterization of High-Speed Electronic Devices using Ultrafast Lasers*. PhD thesis, University of British Columbia. To be submitted.
- [20] F. E. Doany, D. Grischkowsky, and C.-C. Chi, "Carrier lifetime versus ion-implantation dose in silicon on sapphire," *Applied Physics Lett.*, vol. 50, pp. 262–263, February 1987.
- [21] S. Gupta, J. F. Whitaker, and G. A. Mourou, "Ultrafast carrier dynamics in III-V semiconductors grown by molecular-beam epitaxy at very low substrate temperatures," *IEEE Journal of Quantum Electronics*, vol. 28, pp. 2464–2472, October 1992.
- [22] D. H. Auston, K. P. Cheung, and P. R. Smith, "Picosecond photoconducting Hertzian dipoles," *Applied Physics Lett.*, vol. 45, pp. 284–286, August 1984.

- [23] N. Katzenellenbogen and D. Grischkowsky, "Efficient generation of 380 fs pulses of THz radiation by ultrafast laser pulse excitation of a biased metal-semiconductor interface," *Applied Physics Lett.*, vol. 58, pp. 222-224, January 1991.
- [24] M. Y. Frankel, S. Gupta, J. A. Valdmanis, and G. A. Mourou, "Picosecond pulse formation by transmission line discontinuities," *Electronics Lett.*, vol. 25, pp. 1363-1364, September 1989.
- [25] N. G. Paulter, D. N. Sinha, A. J. Gibbs, and W. R. Eisenstadt, "Optoelectronic measurements of picosecond electrical pulse propagation in coplanar waveguide transmission lines," *IEEE Transactions on Microwave Theory and Techniques*, vol. 37, pp. 1612-1619, October 1989.
- [26] M. D. Feuer, S. C. Shunk, P. R. Smith, H. H. Law, and M. C. Nuss, "100 GHz wafer probes based on photoconductive sampling," *IEEE Photonics Technology Lett.*, vol. 5, pp. 361-364, March 1993.
- [27] H. Cheng and J. F. Whitaker, "300-GHz-bandwidth network analysis using time-domain electrooptic sampling," in *1993 IEEE Microwave Theory Tech. Symp. Dig.*, pp. 1355-1358, 1993.
- [28] R. Y. Yu, Y. Konishi, M. Case, M. Kamegawa, and M. Rodwell, "A time-domain millimeter-wave vector network analyzer," *IEEE Microwave and Guided Wave Lett.*, vol. 2, pp. 319-321, August 1992.
- [29] M. Y. Frankel, "500-GHz characterization of an optoelectronic S-parameter test structure," *IEEE Microwave and Guided Wave Lett.*, vol. 4, pp. 118-120, April 1994.
- [30] X. Wu, D. Conn, J. Song, and K. Nickerson, "Invasiveness of LiTaO₃ and GaAs probes in external E-O sampling," *IEEE J. Lightwave Tech.*, vol. 11, pp. 448-454, March 1993.
- [31] A. Zeng, S. A. Shah, and M. K. Jackson, "Reduced invasiveness of non-contact electro-optic probes in millimeter-wave optoelectronic characterization." *IEEE Transactions on Microwave Theory and Techniques* [in press].
- [32] J. Ritter, V. J. Brankovic, D. V. Krupezevic, and F. Arndt, "A wide-band S-parameter extraction procedure for arbitrarily shaped, inhomogeneous structures using time domain numerical techniques," in *1995 IEEE Microwave Theory Tech. Symp. Dig.*, pp. 274-276, 1995.
- [33] Y.-D. Lin, J.-W. Sheen, and C.-Y. Chang, "Surface-wave leakage properties of coplanar strips," in *1993 IEEE Microwave Theory Tech. Symp. Dig.*, pp. 229-231, 1995.

- [34] M. Hatzakis, B. J. Canavello, and J. M. Shaw, "Single-step optical lift-off process," *IBM J. Res. Development*, vol. 24, pp. 452-460, July 1980.

Appendix A

Experimental Device Fabrication

The coplanar transmission line electrodes were fabricated using a chlorobenzene lift-off process to have overhanging lips on the side-walls of the photoresist [34]. Fabrication of metal electrodes involved the following steps:

1. Clean the substrate with acetone and methanol. Blow dry with Nitrogen.
2. Spin on Shipley 1400-27 resist: 5000 rpm for 30 s.
3. Remove edge bead using q-tips and acetone.
4. Soft-bake at 70°C for 20 minutes in oven, cover the sample with petridish.
5. Expose the sample for 20 s with Karl-Suss MJB3 contact mask aligner operating at 320 nm and with nominal intensity.
6. Place the sample in Chlorobenzene for 12 minutes.
7. Post-bake for 15 min at 70°C.
8. Develop using Shipley MF-319 developer for 6 minutes.
9. Rinse the sample by using deionized (DI) Water.
10. Evaporate 30nm/70nm of Cr/Au using E-beam evaporation.
11. Photoresist was dissolved by immersing sample in the acetone. The ultrasonic wasn't normally used to assist lift-off.